Seasonal evolution of Antarctic supraglacial lakes in 2015-2021 and links to environmental controls

Mariel C. Dirscherl[1], Andreas J. Dietz[1], Claudia Kuenzer[1,2]

[1]German Remote Sensing Data Center (DFD), German Aerospace Center (DLR), Muenchener Strasse 20, 82234 Weßling,
5 Germany
[2]Institute of Geography and Geology, University Wuerzburg, Am Hubland, 97074 Wuerzburg, Germany

Correspondence to: Mariel C. Dirscherl (Mariel.Dirscherl@dlr.de)

Abstract. Supraglacial meltwater accumulation on ice shelves may have important implications for future sea-level-rise.
Despite recent progress in the understanding of Antarctic surface hydrology, potential influences on ice shelf stability as well
10 as links to environmental drivers remain poorly constrained. In this study, we employ state-of-the-art machine learning on
Sentinel-1 Synthetic Aperture Radar (SAR) and optical Sentinel-2 satellite imagery to provide new insight into the inter-annual
and intra-annual evolution of surface hydrological features across six major Antarctic Peninsula and East Antarctic ice shelves.
For the first time, we produce a record of supraglacial lake extent dynamics for the period 2015-2021 at unprecedented 10 m
spatial resolution and bi-weekly temporal scale. Through synergetic use of optical and SAR data, we obtain a more complete
15 mapping record enabling the delineation of also buried lakes. Our results for Antarctic Peninsula ice shelves reveal below
average meltwater ponding during most of melting seasons 2015-2018 and above average meltwater ponding throughout
summer 2019-2020 and early 2020-2021. Meltwater ponding on investigated East Antarctic ice shelves was far more variable
with above average lake extents during most of melting seasons 2016-2019 and below average lake extents during 2020-2021.
This study is the first to investigate relationships with climate drivers both, spatially and temporally including time lag analysis.
20 The results indicate that supraglacial lake formation in 2015-2021 is coupled to the complex interplay of varying air
temperature, solar radiation, snowmelt, wind and precipitation, each at different time lags and directions and with strong local
to regional discrepancies, as revealed through pixel-based correlation analysis. Southern Hemisphere atmospheric modes as
well as the local glaciological setting including melt-albedo feedbacks and the firn air content were revealed to strongly
influence the spatio-temporal evolution of supraglacial lakes as well as below or above average meltwater ponding despite
25 variations in the strength of forcing. Recent increases of Antarctic Peninsula surface ponding point towards a further reduction
of the firn air content implying an increased risk for ponding and hydrofracture. In addition, lateral meltwater transport was
observed over both Antarctic regions with similar implications for future ice shelf stability.

1 Introduction

With accelerating global climate change, the Greenland and Antarctic ice sheets are exposed to increasing environmental
30 pressure (Meredith et al., 2019). Recent disintegration of Antarctic Peninsula (API) ice shelves was associated with

atmospheric warming causing extensive meltwater ponding and hydrofracture to initiate ice shelf collapse (Banwell et al., 2013; Bell et al., 2018; Cook and Vaughan, 2010; Leeson et al., 2020; Rignot et al., 2004; Scambos et al., 2004). Ice shelf collapse leads to a reduction in buttressing initiating glacier acceleration and API ice mass loss to increase from 7 ± 13 billion to 33 ± 16 billion tonnes per year in 1992-2017 (Berthier et al., 2012; Rott et al., 2018; The IMBIE Team, 2018). With surface

35   melting expected to double by 2050 (Trusel et al., 2015), Antarctic surface hydrological features will likely expand and become a dominant driver for future ice shelf instability and ice mass loss from the Antarctic (Arthur et al., 2020a; Lai et al., 2020). Apart from the risk of hydrofracture (Fürst et al., 2016; Lai et al., 2020), also an inland migration of lakes could result in ice flow accelerations through the connection of surface and basal hydrological systems leading to basal lubrication and sliding (Bartholomew et al., 2010; Bell et al., 2018; Tuckett et al., 2019). Moreover, melt-albedo feedbacks can contribute to enhanced

40   surface melting near exposed bedrock and blue ice as well as due to the albedo-lowering effect of supraglacial lakes themselves (Arthur et al., 2020a; Bell et al., 2018; Kingslake et al., 2017; Lenaerts et al., 2017). Occurrence of supraglacial meltwater ponding is further promoted in regions of low firn air content (FAC), e.g., due to firn over-saturation, refreezing of lakes or the absence of snowfall (Alley et al., 2018; Arthur et al., 2020a; Kuipers Munneke et al., 2014; Lenaerts et al., 2017; Spergel et al., 2021; Stokes et al., 2019), as well as over topographic undulations and where katabatic or foehn winds prevail (Cape et

45   al., 2015; Datta et al., 2019; Laffin et al., 2021; Lenaerts et al., 2017; Luckman et al., 2014). In addition, ice shelves that are structurally weakened by fractures and crevasses could be more vulnerable to hydrofracture (Lhermitte et al., 2020).

Despite recent advances in the understanding of Antarctic surface hydrology, detailed analyses of the spatio-temporal evolution of Antarctic supraglacial lakes as well as implications for ice shelf stability and links to environmental controls remain poorly constrained. For improved evaluation of seasonal fluctuations of Antarctic surface hydrology as well as

50   associated drivers and impacts, automated mapping methods with spatio-temporal transferability are required. In this context, recent progress in the mapping of Antarctic surface hydrology results from large-scale mapping efforts using optical (Dell et al., 2020; Dirscherl et al., 2020; Halberstadt et al., 2020; Kingslake et al., 2017; Moussavi et al., 2020; Stokes et al., 2019) and Synthetic Aperture Radar (SAR) (Dirscherl et al., 2021) data from spaceborne remote sensing revealing widespread occurrence of surface ponding particularly on the API and East Antarctic Ice Sheet (EAIS) (Arthur et al., 2020a). Employing state-of-the-

55   art machine learning, method developments using Sentinel-1 SAR (Dirscherl et al., 2021) and optical Sentinel-2 data (Dirscherl et al., 2020) enable the generation of fused supraglacial lake extent classification products at high spatial and temporal resolution allowing to exploit and overcome sensor-specific advantages and disadvantages including retrieval of mappings during polar darkness or cloud cover. Providing more complete mapping records than single-sensor classifications, combined Sentinel-1 and Sentinel-2 supraglacial lake extent mappings are the primary data source within the present study. In this

60   context, consideration of SAR imagery enables the detection of also buried lakes.

Exploiting the archive of Sentinel-1 and Sentinel-2, this study aims at (i) investigating seasonal and inter-annual supraglacial lake extent dynamics in 2015-2021 over six major Antarctic ice shelves on the API and EAIS, (ii) analysis of anomalous supraglacial lake occurrence below or above average, (iii) establishing a link between spatio-temporal variability in supraglacial lake occurrence and associated environmental controls including both, the near-surface climate and the local

65 glaciological setting and (v) evaluation of the influence of teleconnections and Southern Hemisphere atmospheric modes on climate and lake extent variability. While it is beyond the scope of this study to identify specific short-term drivers of lake occurrence or absence, we mostly focus on the analysis of climate variability during the entire investigation period 2015-2021.

70

75

80

85
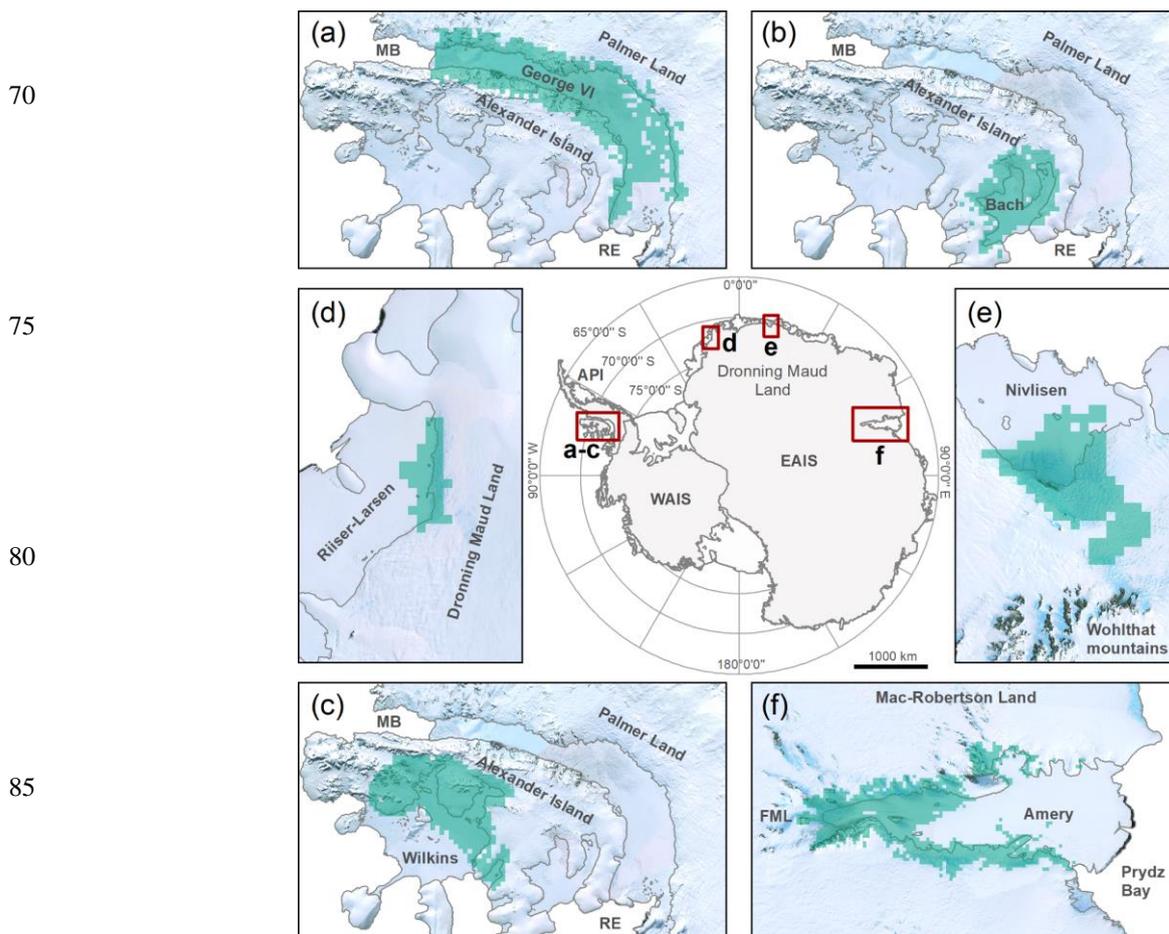
Figure 1 Overview map of Antarctica with the study regions on the Antarctic Peninsula (API) (a-c) and the East Antarctic Ice Sheet (EAIS)
90 (d-f) outlined in in red. The shaded turquoise area in (a-f) delineates the areas of interest. Over Amery Ice Shelf, the large lake feature at the western grounding line was excluded from analyses. The outline of the Antarctic ice sheets is taken from IMBIE (2016) and coastline and grounding line data are from Mouginot et al. (2017) and Rignot et al. (2013). The background in (a-f) is the Landsat Image Mosaic of Antarctica (LIMA) (Bindschadler et al., 2008). MB: Marguerite Bay. RE: Ronne Entrance. FML: Fisher, Mellor and Lambert glacier systems. WAIS: West Antarctic Ice Sheet.

95 2   Study sites

The six major ice shelves investigated in this study are shown in Fig. 1. Of these, three are situated on the southwest API and three are distributed around the margin of the EAIS. The choice of study regions was made in agreement with known supraglacial lake occurrences across different glaciological and climatic settings (Banwell et al., 2021; Dell et al., 2020; Dirscherl et al., 2021; Kingslake et al., 2017; Spergel et al., 2021) as well as satellite data availability. The study regions on

100   the API are located in the Bellingshausen Sea Sector and cover the neighbouring George VI, Bach and Wilkins Ice Shelf (Fig.

1a-c). Separated by Alexander Island (71°00' S, 70°00' W), these ice shelves stretch over an area of ~23 370 km², ~4540 km²,

and ~11 144 km², respectively (Cook and Vaughan, 2010; Holt et al., 2013a). While Bach and Wilkins Ice Shelf are fed by

several inlets from Alexander Island and have comparatively broad calving fronts with respect to their total extent, the

structural setting of George VI Ice Shelf is far more complex (Banwell et al., 2021). Stretching over ~450 km along its

105   centreline and up to ~75 km at its northern and southern calving fronts in Marguerite Bay and Ronne Entrance, George VI Ice

Shelf is located within a narrow channel between Alexander Island and Palmer Land (Holt et al., 2013b). The latter provides

most of the ice inflow onto the ice shelf compressing laterally against Alexander Island (Hambrey et al., 2015; Holt et al.,

2013a; LaBarbera and MacAyeal, 2011; Reynolds and Hambrey, 1988). The structural setting of George VI also influences

its ice motion field reaching peak velocities up to 2.5 m d^{-1} at its eastern grounding line and considerably lower values towards

110   the west (Hogg et al., 2017). In contrast, ice flow velocities on Bach and Wilkins Ice Shelf are comparatively low with maxima

up to ~1 m d^{-1} near their grounding lines (Hogg et al., 2017; Padman et al., 2012). Over recent decades, changes in ice dynamics

along the Bellingshausen Sea Sector were mostly attributed to the local glacier and bedrock geometry as well as Circumpolar

Deep Water upwelling onto the continental shelf leading to enhanced basal melting (Hogg et al., 2017; Minchew et al., 2018;

Rignot et al., 2019). On the other hand, summer surface melting led to the formation of extensive surface hydrological networks

115   over all three ice shelves (Fig. 2a-c) (Banwell et al., 2021; Dirscherl et al., 2021, 2020; Reynolds, 1981; Wagner, 1972).
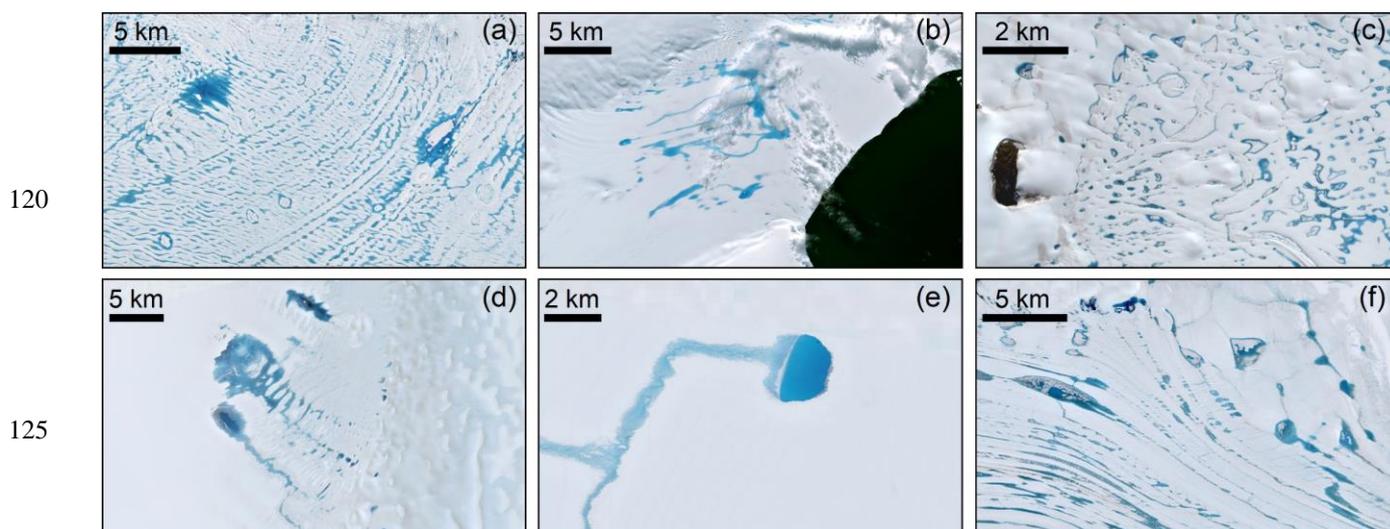
Figure 2 Sentinel-2 optical image extracts (RGB) showing supraglacial lake occurrence on (a) 19 January 2020 over George VI Ice Shelf,
(b) 29 January 2020 over Bach Ice Shelf, (c) 23 January 2021 over Wilkins Ice Shelf, (d) 2 February 2017 over Riiser-Larsen Ice Shelf, (e)
130   21 January 2019 over Nivlisen Ice Shelf and (f) 2 January 2019 over Amery Ice Shelf. Data source: Copernicus Sentinel-2 data.

The three investigated ice shelves on the EAIS include Riiser-Larsen, Nivlisen and Amery Ice Shelf, each stretching over

an area of ~48 180 km², ~7600 km², and ~62 620 km², respectively (Dell et al., 2020; Foley et al., 2013). To start with, Riiser-

Larsen Ice Shelf (Fig. 1d) is located in western Dronning Maud Land (72°40' S, 15°00' W) and is grounded along several

hundred kilometres in parallel to the calving front as well as above several ice rises and pinning points (Kleiner and Humbert,
135   2014). Most of the ice discharge across Riiser-Larsen Ice Shelf originates from the adjacent Plogbreen and Veststraumen ice
streams with ice velocities generally below 1 m d^{-1} (Gardner et al., 2018; Shen et al., 2018). Next, Nivlisen Ice Shelf (Fig. 1e)
lies within the central section of Dronning Maud Land (70°30' S, 11°30' E) and is fed by ice draining through Wohlthat
mountains (Horwath et al., 2006). Its overall ice flow is comparatively slow with peak velocities <0.5 m d^{-1} (Horwath et al.,
2006; Shen et al., 2018). Situated in Mac-Robertson Land, Amery (71°00' S, 70°00' E) is the largest of all East Antarctic ice
140   shelves (Fig. 1f). Amery Ice Shelf is located in Prydz Bay and stretches over a length and width of ~550 km and ~180 km,
respectively. It is nourished by three major glaciers - Fisher, Mellor and Lambert - and reaches peak velocities of 4 m d^{-1} at its
front (Tong et al., 2018). Overall, ice dynamics at Amery, Riiser-Larsen and Nivlisen Ice Shelf remained remarkably steady
over the last decades (Gardner et al., 2018; Rignot et al., 2019; Shen et al., 2018; Tong et al., 2018). At the same time, extensive
networks of supraglacial lakes and streams were observed on all three ice shelves (Fig. 2d-f) (Dell et al., 2020; Dirscherl et al.,
145   2021, 2020; Moussavi et al., 2020; Spergel et al., 2021; Stokes et al., 2019).

In this study, the area of interest (AOI) chosen for each ice shelf region was delineated in agreement with confirmed
supraglacial lake occurrences during at least one time step within our investigation period 2015-2021 as well as on basis of
resampled ERA5-Land pixel footprints (turquoise area in Fig. 1a-f). For George VI, Bach, Wilkins, Riiser-Larsen, Nivlisen
and Amery Ice Shelf, this resulted in AOI subsets of 27 324 km^2, 9504 km^2, 15 660 km^2, 1512 km^2, 5292 km^2, and 41 760
150   km^2, respectively. Where lake coverage expanded inland across the grounding lines, the adjacent grounded ice was included
explaining the partly larger AOI sizes compared to the corresponding ice shelf areas.

3   Materials and methods

3.1   Datasets

3.1.1   Satellite imagery

155   For automated mapping of Antarctic supraglacial lake extents, we jointly use Sentinel-1 and Sentinel-2 satellite imagery. The
Sentinel-1 SAR data used in this study were acquired in interferometric wide (IW) swath mode delivering data products at 10
m pixel spacing and in horizontal transmit and receive polarization (HH). For each study region, we acquired all available
Sentinel-1 data covering the period 1 November to 31 March in 2015-2021 within pre-defined boundaries including the six ice
shelves as well as surrounding grounded area. Over Riiser-Larsen, Nivlisen and Amery Ice Shelf, data availability during
160   melting season 2015-2016 was not sufficient restricting the Sentinel-1 data selection to the period 2016-2021. In contrast,
Sentinel-1 data over George VI, Bach and Wilkins Ice Shelf were available during all melting seasons 2015-2021. Overall,
this resulted in a total number of 3075 Sentinel-1 acquisitions covering all six study regions.

Regarding optical Sentinel-2 data, we selected all imagery with a scene cloud cover <75 % available within the same pre-
defined time frame and boundaries as defined for Sentinel-1. This comparatively high cloud threshold was chosen in order to
165   obtain the most complete record of supraglacial lake occurrence also during months when high cloud cover prevails in parts

of the image scenes. Moreover, cloud masking procedures over glaciated regions are often impacted by the appearance of ice similar to clouds thus indicate higher cloud coverage than is present in the actual acquisitions resulting in an incomplete data record. Considering these filtering criteria, a total of 2167 Sentinel-2 acquisitions was gathered for all six study regions within the period November to March in 2015-2021.

3.1.2   ERA5-Land reanalysis data

For analysis of climatological controls on Antarctic supraglacial lake occurrence in 2015-2021, we use hourly ERA5-Land atmospheric reanalysis data (Munoz Sabater, 2019). ERA5-Land replaces the former ERA-Interim product of the European Centre for Medium-Range Weather Forecasts (ECMWF) and provides reanalysis data for a variety of land variables at a spatial resolution of 0.1° (~9 km) as well as a temporal coverage dating back to 1981. The use of large-scale reanalysis data compared to ground-based observations, e.g., from local weather stations is particularly beneficial over Antarctica due to its vast size and remote geographical location complicating detailed ground-based monitoring efforts.

The ERA5-Land variables used in this study include 2 m air temperature, surface net solar radiation, wind, total precipitation, as well as snowmelt. Data were retrieved for the period 1 October to 1 March of each melting season in 2015-2021 whereat October and November data were included for evaluation of potential time lag effects of climate variables. For precipitation data, we additionally retrieved hourly estimates for all remaining months in 2015-2020 in order to allow the evaluation of links between previous year precipitation and supraglacial lake formation. To start with, ERA5-Land temperature data provide the best estimate of the seasonal cycle of near-surface temperature over coastal Antarctica and particularly the API compared to other existing reanalysis datasets (Gossart et al., 2019; Tetzner et al., 2019). ERA5-Land temperature data outperform other reanalysis datasets considering its low bias and low mean absolute error of 2° C over Antarctica (Gossart et al., 2019). On the other hand, surface net solar radiation represents the difference between downward solar (or shortwave) radiation incident upon the Earth's surface and the amount of radiation reflected back to space. To date, data on surface net solar radiation have not been validated over Antarctica while studies over China and Europe point towards an improved performance of ERA5 radiation components compared to other reanalysis datasets (Jiang et al., 2020; Urraca et al., 2018). Next, ERA5-Land wind data are provided at 10 m above the surface as the horizontal speed of air moving towards the north and east, respectively. ERA5-Land wind data were revealed to capture the typical annual cycle of wind with a mean underestimation during winter when katabatic wind forcing is strongest (Gossart et al., 2019). Similarly, a slight underestimation of wind magnitude was observed over coastal Antarctica during summer resulting in an overall mean absolute error of 2.8 m s^{-1} (Gossart et al., 2019). Estimates of ERA5-Land total precipitation are provided in metres depth and include all liquid and frozen water accumulated at the Earth's surface. Overall, ERA5-Land precipitation data perform well in detecting precipitation events over the API even though a bias may exist, e.g., due to the negligence of effects such as the redeposition of snow (Tetzner et al., 2019). Finally, ERA5-Land modelled snowmelt data are available in metres of water equivalent. As no evaluation of the ERA5-Land snowmelt product exists for the Antarctic continent, the data should be handled with care.

3.2 Methods

3.2.1 Pre-processing and data preparation

200 The satellite data were pre-processed using sensor-specific processing tools. For Sentinel-1 SAR data, we used the open source
Sentinel Application Platform (SNAP). Pre-processing of Sentinel-1 SAR imagery includes orbit correction, thermal noise
removal, radiometric calibration, speckle filtering as well as terrain correction. For the latter, the TanDEM-X PolarDEM 90
of Antarctica (Wessel et al., 2021) was used. In order to prepare the data for prediction of supraglacial lakes (see Sect. 3.2.2),
each pre-processed Sentinel-1 image was normalised and tiled into 480 x 480-pixel patches with 200-pixel overlap (Dirscherl
205 et al., 2021). In contrast, optical Sentinel-2 data required correction for atmospheric effects using Sen2Cor, a processor for
retrieval of surface reflectance (Louis et al., 2016). Moreover, selected indices needed for image classification (Dirscherl et
al., 2020) were calculated and all bands and indices resampled to the highest resolution of available Sentinel-2 bands (10 m).

Pre-processing of ERA5-Land data included a range of individual processing steps for each variable. At first, hourly
estimates of ERA5-Land air temperature were resampled to daily averages and temperature measured in Kelvin was converted
210 to degree Celsius (°C). Next, hourly data on surface net solar radiation were converted to average daily energy fluxes in watts
per square meter (W m^{-2}). On the other hand, hourly zonal (u) and meridional (v) wind stress components at 10 m above the
surface were used to derive daily averages of zonal and meridional wind stress to be converted to wind magnitude ($w_m = \sqrt{u^2 + v^2}$) and direction ($w_d = 180 + (\arctan(v, u) * 180/\pi)$) following aggregation to bi-weekly averages (see Sect.
3.2.3). For calculation of daily total precipitation, we considered the total accumulated value of a day and converted to
215 millimeters depth. Finally, daily snowmelt information was obtained from hourly snowmelt data through consideration of the
total accumulated value of a day and conversion to millimeters of water equivalent. All obtained daily ERA5-Land data were
reprojected to the Antarctic Polar Stereographic projection in order to allow comparison to lake extent mappings.

3.2.2 Automated supraglacial lake extent mapping

For prediction of supraglacial lake extents in normalised Sentinel-1 image patches, we use a Convolutional Neural Network
220 (CNN) based on residual U-Net (Dirscherl et al., 2021). In detail, a standard U-Net architecture was complemented with
residual connections as well as an Atrous Spatial Pyramid Pooling (ASPP) module for improved performance. In this context,
the choice of a deep learning network over traditional image processing techniques was mainly made due to the similar
appearance of Antarctic supraglacial lakes and surface features such as wet snow, blue ice or topographic shadow in single-
polarized SAR imagery but also due to effects such as wind roughening and speckle noise (Dirscherl et al., 2021). Model
225 training was performed on basis of 21 200 Sentinel-1 image patches extracted from 58 Sentinel-1 image scenes covering
melting seasons 2018-2019 and 2019-2020 over 13 different Antarctic regions. Following semantic segmentation of the image
patches, the resultant prediction probability maps were reshaped into their original image size and thresholded. In particular,
all pixels above a probability threshold of 0.5 were accepted as supraglacial lake pixels. As part of post-processing, remaining
errors in the binary classification maps were reduced applying morphological filtering as well as topographic and coastline

230   masking using a resampled version of the TanDEM-X PolarDEM as well as a dilated Sentinel-1 coastline product of 2018
       (Baumhoer et al., 2021). The performance of the Sentinel-1 classification approach was evaluated over ten independent test
       sites suggesting the good functionality of the algorithm with an average F_1-score of 93 % for all regions. The F_1-score is a
       common statistical accuracy metric reflecting the harmonic mean of the rate of true positive pixels with respect to all true class
       samples and the rate of true positive pixels with respect to all predicted class samples (Jolly, 2018; Müller and Guido, 2016).
235   Remaining limitations are mostly related to false positive lake classifications over radar shadow, wet snow or blue ice.

       Supraglacial lake classification in optical Sentinel-2 imagery was performed using an advanced version of the machine
       learning algorithm published in Dirscherl et al. (2020). In detail, the algorithm is based upon a Random Forest (RF) classifier
       trained on selected Sentinel-2 bands and indices covering 14 different Antarctic regions during three austral summers as well
       as topographic variables derived from the Antarctic TanDEM-X DEM. Similar as for Sentinel-1, post-classification involved
240   bands, indices, topographic and coastline masking as well as morphological erosion. The main modifications in the advanced
       version of the RF algorithm include (i) the integration of more training data over shadow, (ii) the improvement of post-
       classification, e.g., through fine-tuning of variable thresholds and (iii) the use of prediction probability maps for efficient slush
       elimination. Overall, this classification strategy returned an average F_1-score of ~95 % for 14 independent Antarctic test sites.
       Remaining limitations of the classification method include difficulties in detecting mixed pixels at lake edges as well as errors
245   over shadow. Yet, errors due to shadow mainly affect acquisitions towards the end of a summer season when the incidence
       angle of the sun is lower. Furthermore, the discrimination between open water and slightly frozen lakes (e.g., Fig. 2d-e) remains
       challenging. For this reason, we restrict our analysis to supraglacial lake extent derivation and do not calculate lake volumes.
       To support analyses of local controls on lake ponding, we also derive mappings of rock using the modified RF algorithm.

3.2.3   Time series generation and statistical analysis

250   Following supraglacial lake extent mapping, we aggregated all data to bi-weekly time series. To start with, Sentinel-1 and
       Sentinel-2 classification products were combined to maximum lake extent classifications for each bi-weekly time interval
       between November and March of a melting season. To interpolate data gaps over Riiser-Larsen and Nivlisen Ice Shelf (Fig.
       S1d-e), we used the respective long-term mean at bi-weekly scale. Since data gaps were mostly present for months of low lake
       coverage, this interpolation strategy was considered acceptable. For analysis of environmental controls on Antarctic
255   supraglacial lake occurrence, we converted the bi-weekly lake extent time series to fractional water coverage considering
       ERA5-Land grids as AOIs (see Fig. 1). Similarly, the daily ERA5-Land data were aggregated to average bi-weekly time series
       and the grid values over the AOIs extracted. For temperature, we also calculated bi-weekly maxima to capture temperature
       extreme events and positive degree days resulting in seven climate variables used for statistical analysis. In order to investigate
       drivers of anomalous meltwater ponding and to analyse where above or below normal climatic conditions result in above or
260   below normal lake formation with respect to the investigation period 2015-2021, we additionally converted the bi-weekly
       fractional lake extent and climate time series to time series of anomalies. In this study, anomalies are calculated with respect
       to the long-term mean of each bi-weekly time interval. Finally, for joint analysis of January lake extents and total precipitation

in a year preceding lake coverage, we extracted the corresponding aggregates and grid values over each study region. In this study, previous year precipitation was used as indirect indicator for the FAC of snow thus, for analysis of relationships between

265 supraglacial lake formation and the state of the snowpack. Additionally, January lake extents were considered for evaluation of the inter-annual recurrence of lakes both, spatially and temporally supporting the investigation of controls on supraglacial lake formation.

To establish a link between environmental variables and fractional lake extents, we use the Pearson correlation. Pearson's correlation coefficient (r) measures the linear relationship between two variables, where r lies in the range of -1 to +1 reflecting

270 a strong negative and strong positive linear relationship, respectively. Calculation of r also raises the p-value (p), an indicator for statistical significance of correlations. In this study, significance levels of $p<0.05$ (*), $p<0.01$ (**) and $p<0.001$ (***) were defined. In order to obtain more robust correlation values, the bi-weekly statistical analysis was restricted to summer months (December, January and February) when lake coverage is highest and data gaps and classification errors are lowest. Apart from correlating multi-temporal observations of fractional lake extents and climate variables at identical time steps (lag 0), we

275 performed cross-correlation with climate data at time lags 1-4 with each individual lag representing a shift of half a month with respect to the previous lag. These lags capture climatic conditions up to two months preceding a summer season. Considering the investigation periods December to February 2015-2021 and 2016-2021, each individual time series consisted of 36 (API) and 30 (EAIS) observations. Correlation of multi-temporal observations was performed with spatial averages, anomalies of spatial averages as well as pixel-based values. Additionally, fluctuations in annual Southern Annular Mode

280 (SAM) (Marshall, 2018, 2003) and previous year precipitation were correlated with January fractional lake extents based on six (API) and five (EAIS) observations.

4 Results

4.1 Supraglacial lake extent dynamics

4.1.1 Antarctic Peninsula ice shelves

285 As shown in Fig. 3a-c, supraglacial lake extents on the API varied strongly both, inter-annually and intra-annually. For George VI, Bach and Wilkins Ice Shelf, supraglacial lake extents were highest during the second half of January 2020 reaching peak values of ~805 km², ~110 km² and ~45 km², respectively. For years with high supraglacial lake coverage, we observe a rapid onset of supraglacial lake formation in late January except for George VI Ice Shelf, where the 2019-2020 onset was already in early January. Over all three study regions, supraglacial lake coverage started to reduce significantly during the first or second

290 half of February. Regarding calculation of intra-annual anomalies (Fig. 4a-c), a similar pattern can be observed. In detail, all ice shelves were characterised by anomalous high lake extents during the past two melting seasons and anomalous low lake extents in most preceding years. More specifically, lake extents during the 2019-2020 and 2020-2021 melting season were above average during their peak and slightly below average in parts of early 2019-2020 and late 2020-2021.

Moreover, Fig. 5a-f illustrates the annual recurrence of lakes during January. As can be seen, supraglacial lakes on Bach and Wilkins Ice Shelf are clustered closer to the grounding line than on George VI, where lakes stretched over vast parts of the ice shelf during the last two melting seasons . This is also reflected in a low recurrence time of lakes reaching 1-2 years over the central ice shelf. Further, supraglacial lakes on George VI Ice Shelf are clustered closer to the grounding line and rock outcrop in years with low supraglacial lake coverage (see Fig. 5a-c), reflected in higher recurrences of lakes up to 5-6 years.
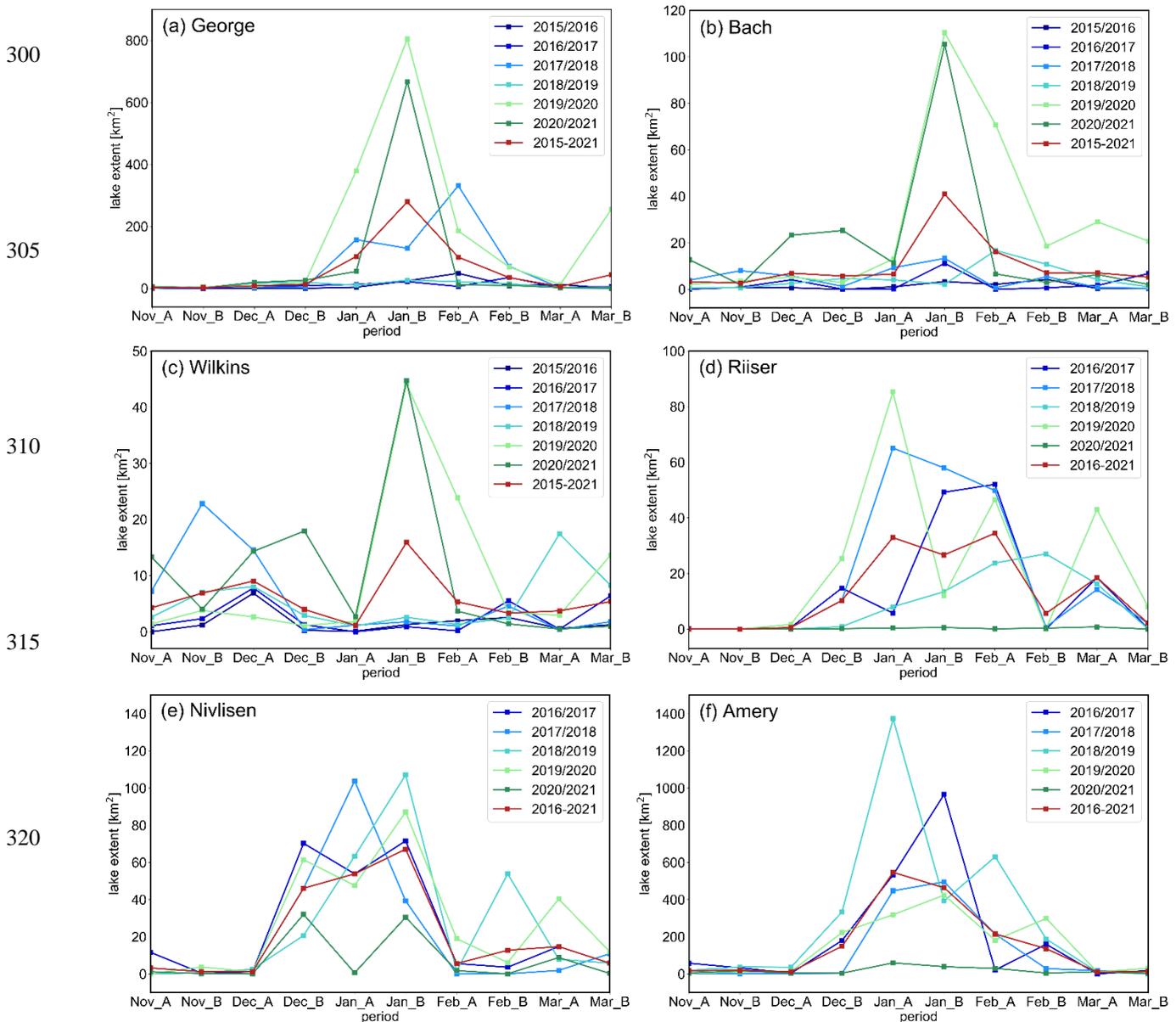
Figure 3 Supraglacial lake extent dynamics over (a) George VI, (b) Bach, (c) Wilkins, (d) Riiser-Larsen, (e) Nivlisen and (f) Amery Ice Shelf, as computed with Sentinel-1 and Sentinel-2 imagery applying state-of-the-art machine learning. The red line in each plot represents the dynamic long-term mean for each respective time interval. The periods represent the bi-weekly time intervals during a melting season with "A" representing the first half of a given month and "B" the second half.
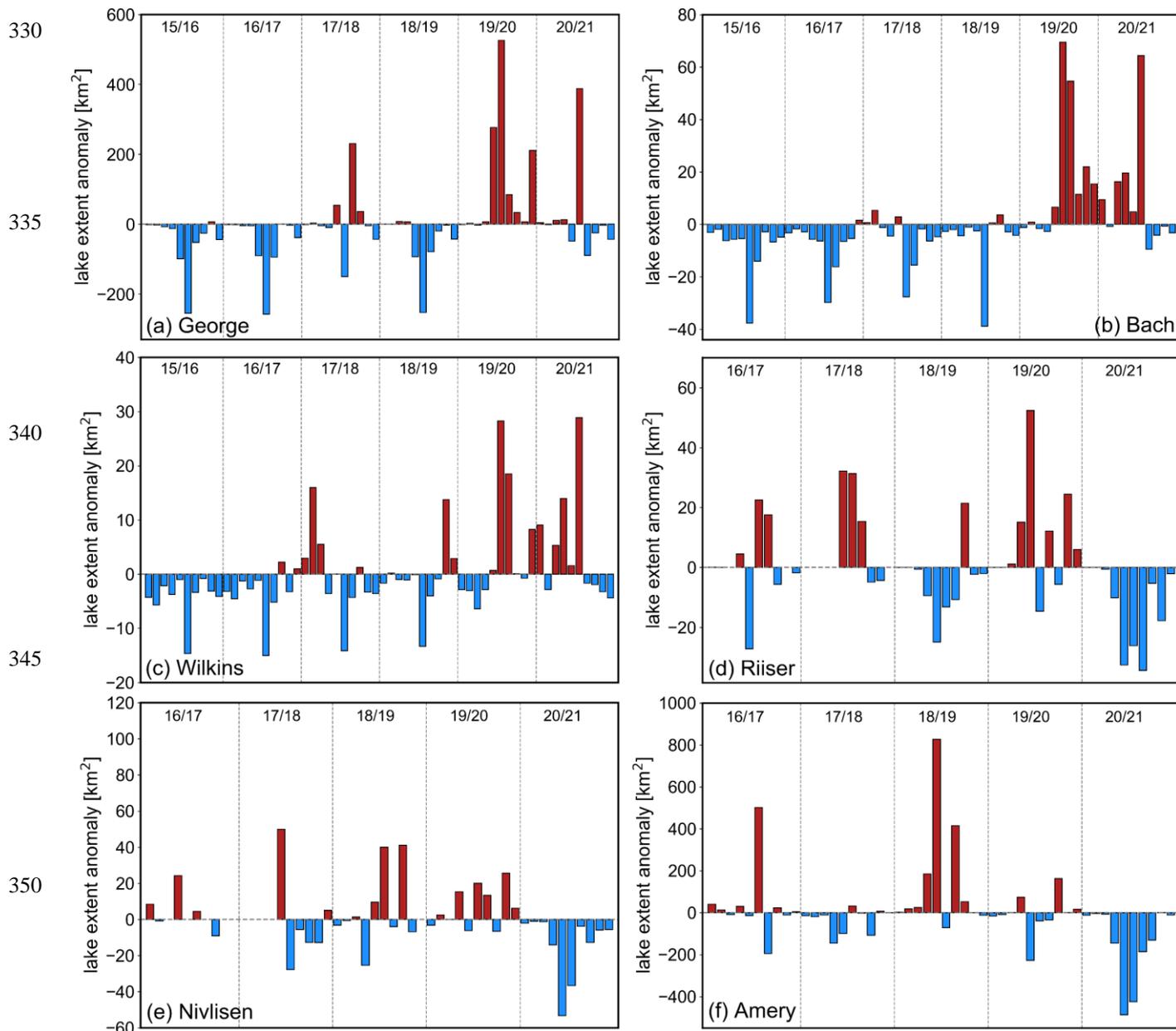
Figure 4 Intra-annual supraglacial lake extent anomalies over (a) George VI, (b) Bach, (c) Wilkins, (d) Riiser-Larsen, (e) Nivlisen and (f) Amery Ice Shelf, as calculated with respect to the long-term mean of each bi-weekly time interval within the investigation period 2015-2021. For Riiser and Nivlisen Ice Shelf, data gaps are visible due to interpolation with the bi-weekly long-term mean. Each bar represents a bi-weekly time interval within the period November to March of an individual melting season. Melting seasons are outlined through separation with dashed grey lines.

4.1.2   East Antarctic ice shelves

360   Supraglacial lake extent dynamics on the EAIS (Fig. 3d-f) differ from the pattern observed for the API. In detail, lake evolution over Riiser-Larsen Ice Shelf fluctuated strongly throughout the melting seasons with the highest observed supraglacial lake extent measured at ~85 km^2 during the first half of January 2020. The highest supraglacial lake extents over Nivlisen (~107 km^2) and Amery (~1373 km^2) Ice Shelf were observed in late and early January 2019, respectively. Over all three ice shelves, lowest supraglacial lake coverage was found for melting season 2020-2021. These patterns are also reflected in the calculation

365   of supraglacial lake extent anomalies (Fig. 4d-f) revealing anomalous high lake extents during parts of melting seasons 2016-2019 and anomalous low lake extents throughout 2020-2021 over Riiser-Larsen and Nivlisen Ice Shelf. Over Amery Ice Shelf, supraglacial lake extents were above average during parts of melting seasons 2016-2017, 2018-2019 and 2019-2020 and below average during most of 2017-2018 and the entire melting season 2020-2021. Moreover, the average onset of EAIS supraglacial lake formation was in late December with lakes persisting longer throughout the melting seasons.

370   Finally, the annual recurrence of lakes during January uncovered clustered supraglacial lake occurrence near the grounding line of Riiser-Larsen Ice Shelf (Fig. 5g-h), lakes spreading across Nivlisen Ice Shelf (Fig. 5i-j) as well as widespread lake occurrence in the southern and eastern sections of Amery Ice Shelf (Fig. 5k-l). During years of peak lake occurrence, lakes expanded further onto the ice shelves while years with lower lake coverage were characterised by lakes clustering closer to the grounding lines. Over all three ice shelves, the January recurrence of lakes reached up to 4-5 years.

375   ## 4.2   Multi-temporal correlation analysis

4.2.1   Correlation analysis with spatial averages

Figure 6 presents the results of the statistical correlation analysis between climate variables and fractional lake extents. To start with, lake extents over George VI Ice Shelf correlate significantly with average and maximum air temperature at time lag 1 (r=0.51** and r=0.40*) as well as with solar radiation at time lag 2 (r=0.43**) (Fig. 6a). Similarly, significant lag 1 correlation

380   was found for anomalies of average and maximum air temperature (r=0.45** and r=0.38*) (Fig. 6b). As detected for George VI Ice Shelf, correlation analysis over Bach Ice Shelf indicates a significant positive relationship with average air temperature at time lag 1 (r=0.40*). At the same time, correlation of anomalies raised significant correlations at lag 0 for both, average and maximum air temperature (r=0.40*, r=0.37*). Over Bach Ice Shelf, also surface melt and anomalies thereof correlate at lag 2 (r=0.40**) and lag 0 (r=0.46***), respectively. While we found no significant correlation for bi-weekly averages over Wilkins

385   Ice Shelf, anomalies of average and maximum air temperature correlate highest at lag 1 (r=0.45**) and lag 0 (r=0.34*), respectively. Besides, anomalies of solar radiation and wind direction correlate negatively at lag 1 (r=-0.36* and r=0.39*) and anomalies of surface melt highest at lag 4 (r=0.42**).
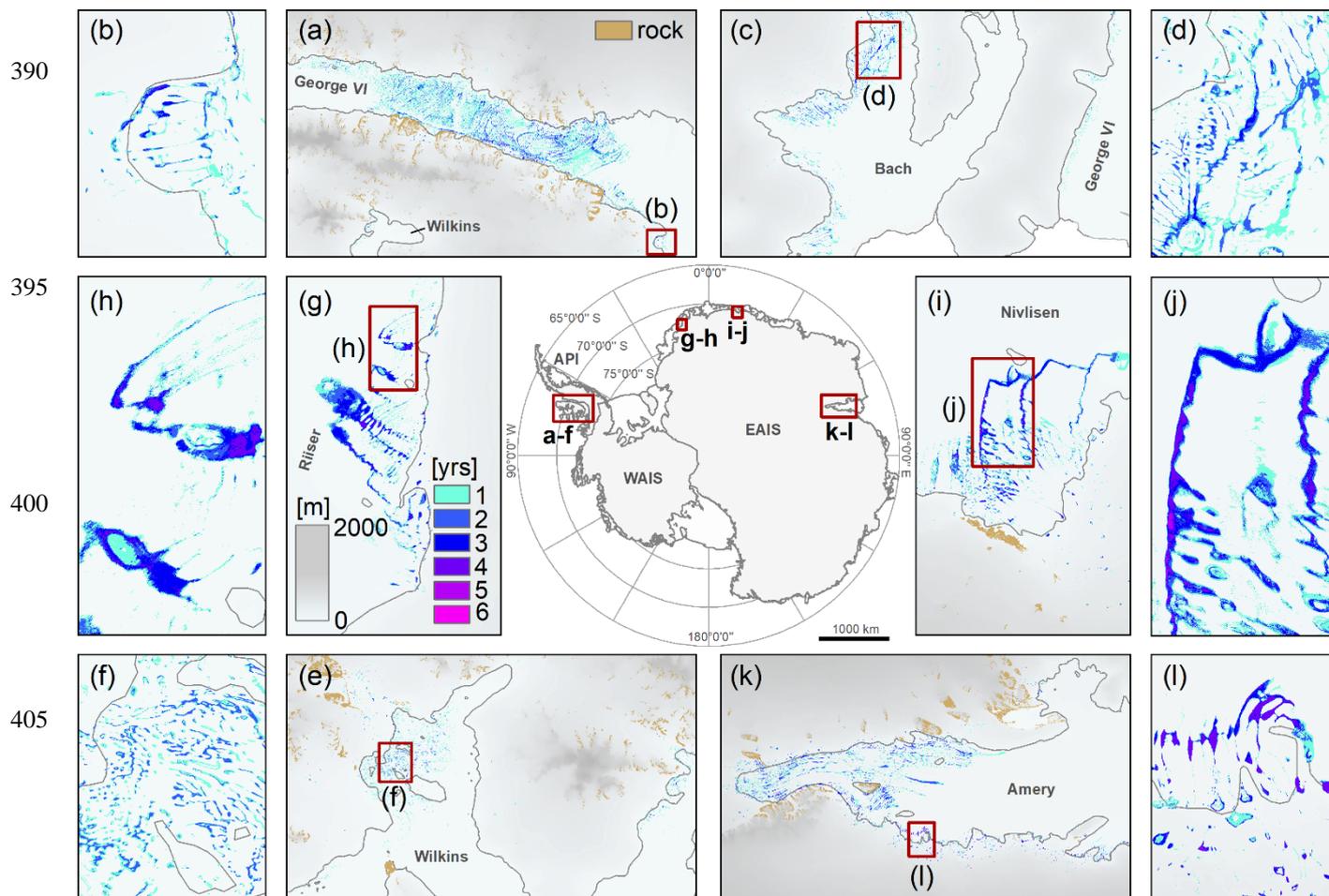
Figure 5 Inter-annual January recurrence of supraglacial lakes over George VI (a-b), Bach (c-d), Wilkins (e-f), Riiser-Larsen (g-h), Nivlisen (i-j) and Amery Ice Shelf (k-l). The overview map in the middle shows the approximate location of the AOIs. The outline of the Antarctic ice sheets is taken from IMBIE (2016), the coastline and grounding line (grey) data are from Mouginot et al. (2017) and Rignot et al. (2013) and Sentinel-2 bedrock data are from Dirscherl et al. (2020). The background elevation is the gap-filled 200 m Reference Elevation Model of Antarctica (Howat et al., 2019). In some regions, the movement of lakes with ice flow might have biased the calculation of annual lake recurrence times. API: Antarctic Peninsula. WAIS: West Antarctic Ice Sheet. EAIS: East Antarctic Ice Sheet.

Linear correlation analysis over Riiser-Larsen Ice Shelf returned a significant positive lag 2 relationship with average air temperature (r=0.57**) and anomalies (r=0.44*). Likewise, solar radiation correlates positively at lag 2 (r=0.42*) and anomalies at lag 0 (r=0.42*). In contrast, significant negative lag 0 correlation was found for precipitation and wind magnitude considering both, average observations (-0.54** and -0.57**) and anomalies (-0.45* and -0.42*). Further, wind direction and anomalies correlate positively at lag 0 (r=0.66*** and r=0.59***) and surface melt and anomalies at lag 1 (r=0.38* and r=0.35*). Statistical analysis over Nivlisen Ice Shelf returned significant correlation with average and maximum air temperature at lag 1 and lag 0 (r=0.58*** and r=0.48**) while solar radiation showed highest correlation at lag 2 (r=0.60***). Moreover, wind direction correlates negatively at lag 1 (r=-0.41*). Anomalies of average and maximum air temperature

correlate strongest at lag 0 (r=0.44*) and lag 1 (r=0.46*) and anomalies of surface melt at lag 4 (r=-0.39*). Finally, correlation
425   analysis over Amery Ice Shelf indicates significant positive relationships with average (r=0.58***) and maximum (r=0.45*)
air temperature at lag 1 as well as with solar radiation at lag 2 (r=0.57***). In contrast, correlation of anomalies highlights a
significant negative relationship with maximum air temperature (r=-0.44*) and highest positive linear relationship with solar
radiation at lag 4 (r=0.58***). In addition, surface melt and anomalies correlate positively at lag 1 (r=0.65*** and 0.42*).

Besides, correlation with annual SAM (Table 1) indicates a significant negative linear relationship (r=-0.82*) over George
430   VI Ice Shelf. Likewise, correlation over Bach and Wilkins Ice Shelf reveals a Pearson coefficient of -0.78 and -0.74. Over
EAIS ice shelves, r values are comparatively low with Riiser-Larsen, Nivlisen and Amery returning correlations of -0.48, 0.10
and 0.44. Regarding correlation with previous year precipitation (Table 1), we find significant relationships over Amery Ice
Shelf (r=-0.87*), lower negative correlation with p>0.05 over George VI (r=-0.35), Bach (r=-0.22), Wilkins (r=-0.36) and
Riiser-Larsen (r=-0.40) Ice Shelf and low positive correlation over Nivlisen Ice Shelf (r=0.17).

435   **4.2.2   Correlation analysis at pixel-level**

Figure 7-8 illustrate selected results for pixel-based correlations, selected on basis of Fig. 6. Remaining pixel-based
correlations can be found in the Supplement (Fig. S2, Fig. S3). In detail, the figures show only significant pixels with the
highest correlations considering all performed cross-correlations as well as the corresponding lags. Pixel-based correlation
over George VI Ice Shelf revealed positive relationships for temperature, solar radiation, wind direction and snowmelt (Fig.
440   7a-h). Air temperature and solar radiation correlate highest in the central ice shelf section at lag 1 and lag 2, respectively, while
lower lags of 0 and 0-1 dominate near the grounding line. Snowmelt and wind direction correlate more heterogeneously with
highest positive values towards the central south for snowmelt and along the eastern grounding line for wind direction. At the
same time, wind direction correlates negatively in the west. Statistical analysis over Bach Ice Shelf (Fig. 7i-p) implies
predominant positive correlations for temperature, solar radiation, wind direction and surface melt at lags 0-1, 2-3, 3-4 and 0-
445   1. In detail, air temperature, solar radiation and snowmelt correlate highest towards the north and west and wind direction
correlates positively in the east and negatively in the west. Spatial correlations over Wilkins Ice Shelf (Fig. 7q-x) were rather
heterogeneous with temperature, wind direction and snowmelt showing positive correlations at lags 0-1, 2-4 and 0-1.

Over Riiser-Larsen Ice Shelf (Fig. 8a-h), positive correlation was found for average air temperature. Lags are dominant at
1-2 with the latter appearing closer to the front. Moreover, positive correlation was found for solar radiation at lags 0-2 and
450   negative correlation for wind and precipitation at lag 0. Statistical analysis over Nivlisen Ice Shelf (Fig. 8i-p) shows significant
positive linear relationships for all variables. Air temperature and solar radiation correlate highest towards the north-west while
wind and precipitation correlate mostly in the south-west. Time lags for wind and precipitation are dominant at lag 4 while
temperature and solar radiation correlate highest at lags 0-1 and 0-2. Regarding temperature, lag 0 is dominant inland of the
grounding line and lag 1 over the ice shelf area. For solar radiation, correlations at lag 0-1 dominate inland of the grounding
455   line and at lag 2 over the ice shelf. Over Amery Ice Shelf (Fig. 8q-x), significant positive correlation was identified for average
air temperature. Here, lag 1 dominates over the central ice shelf and lag 0 along the southern and eastern grounding zone. A

similar pattern is observed for solar radiation where lag 1 prevails in the south and east and lag 2 over the central ice shelf. Analysis of precipitation implies fewer correlations and wind speed correlates along the eastern grounding zone.

Finally, Fig. 9 outlines the spatial correlation pattern between previous year precipitation and January fractional lake

460   extents. As correlations result from only few observations potentially leading to unreliable values of p, also correlations with p>0.05 are shown. As can be seen, previous year precipitation correlates negatively over George VI, Bach, Wilkins, Riiser-Larsen and particularly Amery Ice Shelf. In contrast, correlations over Nivlisen are mostly positive.

Table 1 Results of the statistical correlation analysis between fractional lake extents and previous year precipitation as well as annual Southern Annular Mode (SAM) with r reflecting the Pearson correlation and p the p-value describing statistical significance. Due to the low
465   number of observations used for correlation, the p-value might not be representative and rather r should be used for interpretation.

Variable	Precipitation		SAM	
Statistical parameter	r	p	r	p
George VI	-0.35	0.50	-0.82*	0.04
Bach	-0.22	0.68	-0.78	0.07
Wilkins	-0.36	0.48	-0.74	0.09
Riiser-Larsen	-0.40	0.51	-0.48	0.42
Nivlisen	0.17	0.79	0.10	0.87
Amery	-0.87*	0.05	0.44	0.46
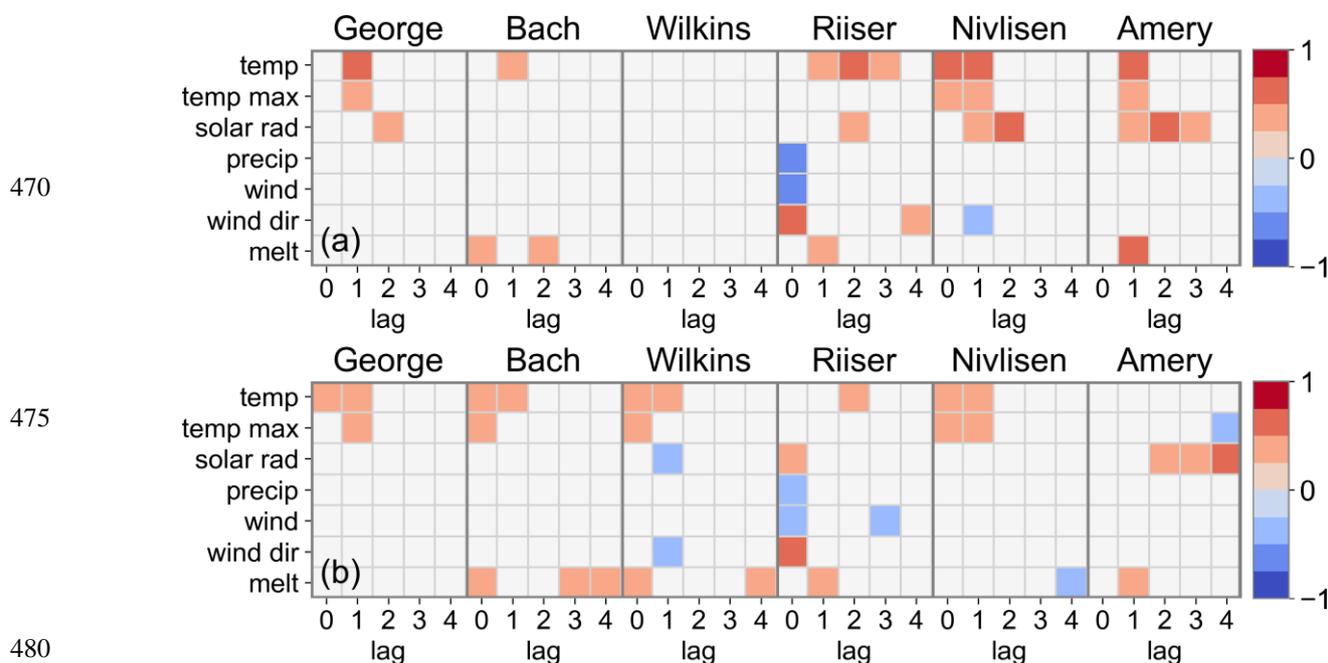
Figure 6 (a) Results of the statistical correlation analysis between fractional lake extents and climate variables air temperature (temp), maximum air temperature (temp max), solar radiation (solar rad), precipitation (precip), wind magnitude (wind), wind direction (wind dir) and snowmelt (melt) at time lags 0-4 over George VI, Bach, Wilkins, Riiser-Larsen, Nivlisen and Amery Ice Shelf. (b) Results of the statistical correlation analysis between anomalies of fractional lake extents and anomalies of climate variables. The correlation coefficient
485   is given in the interval [-1, +1] and is illustrated for significant correlations with p<0.05 only. Correlations with p>0.05 are masked.
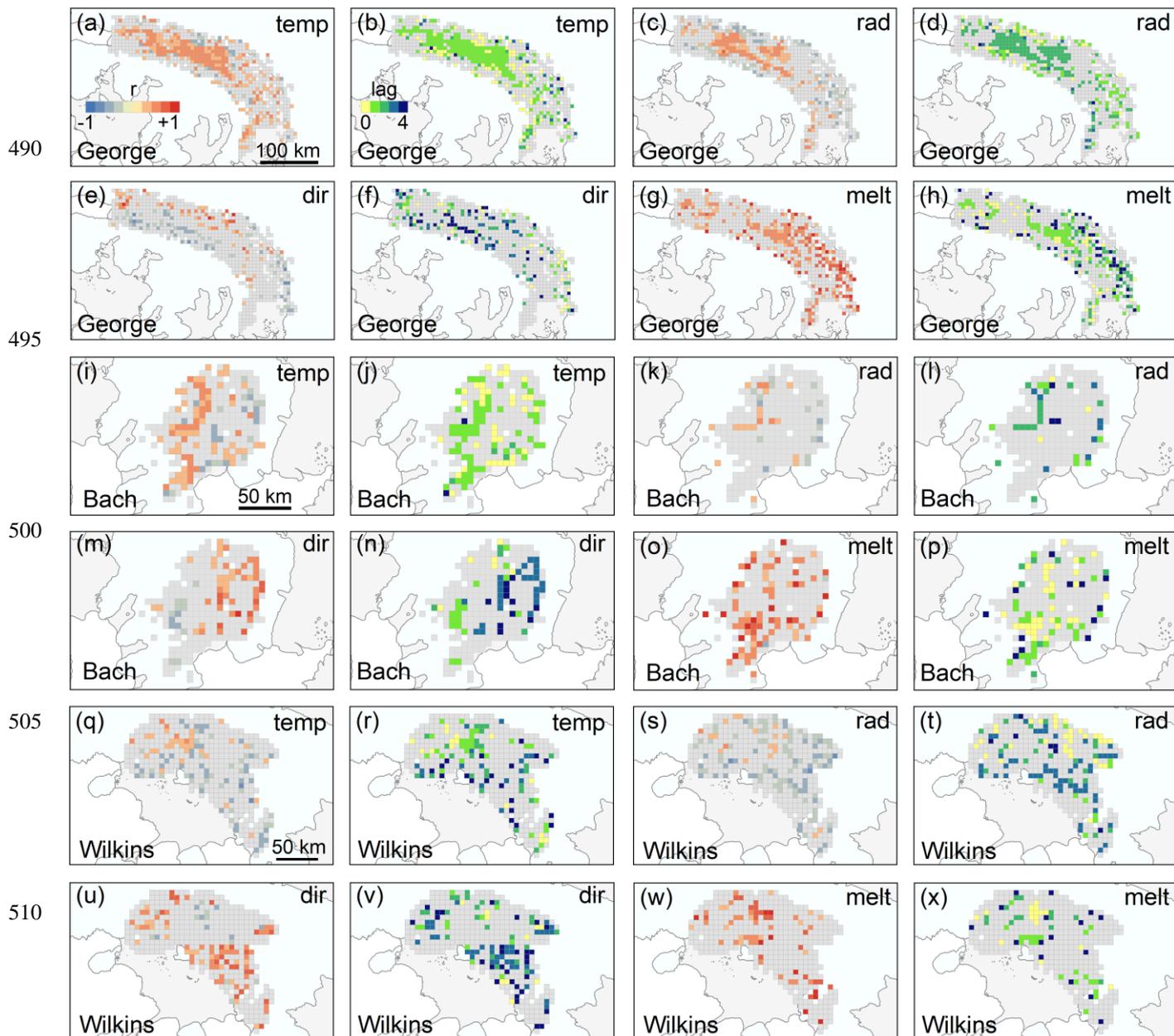
Figure 7 Pixel-based Pearson correlations (r) (a,c,e,g,i,k,m,o,q,s,u,w) and corresponding temporal lags (b,d,f,h,j,l,n,p,r,t,v,x) between fractional lake extents and climate variables air temperature (temp), solar radiation (rad), wind direction (dir) and snowmelt (melt) over the API ice shelves George VI (a-h), Bach (i-p) and Wilkins (q-x). Pixels with p>0.05 are masked.
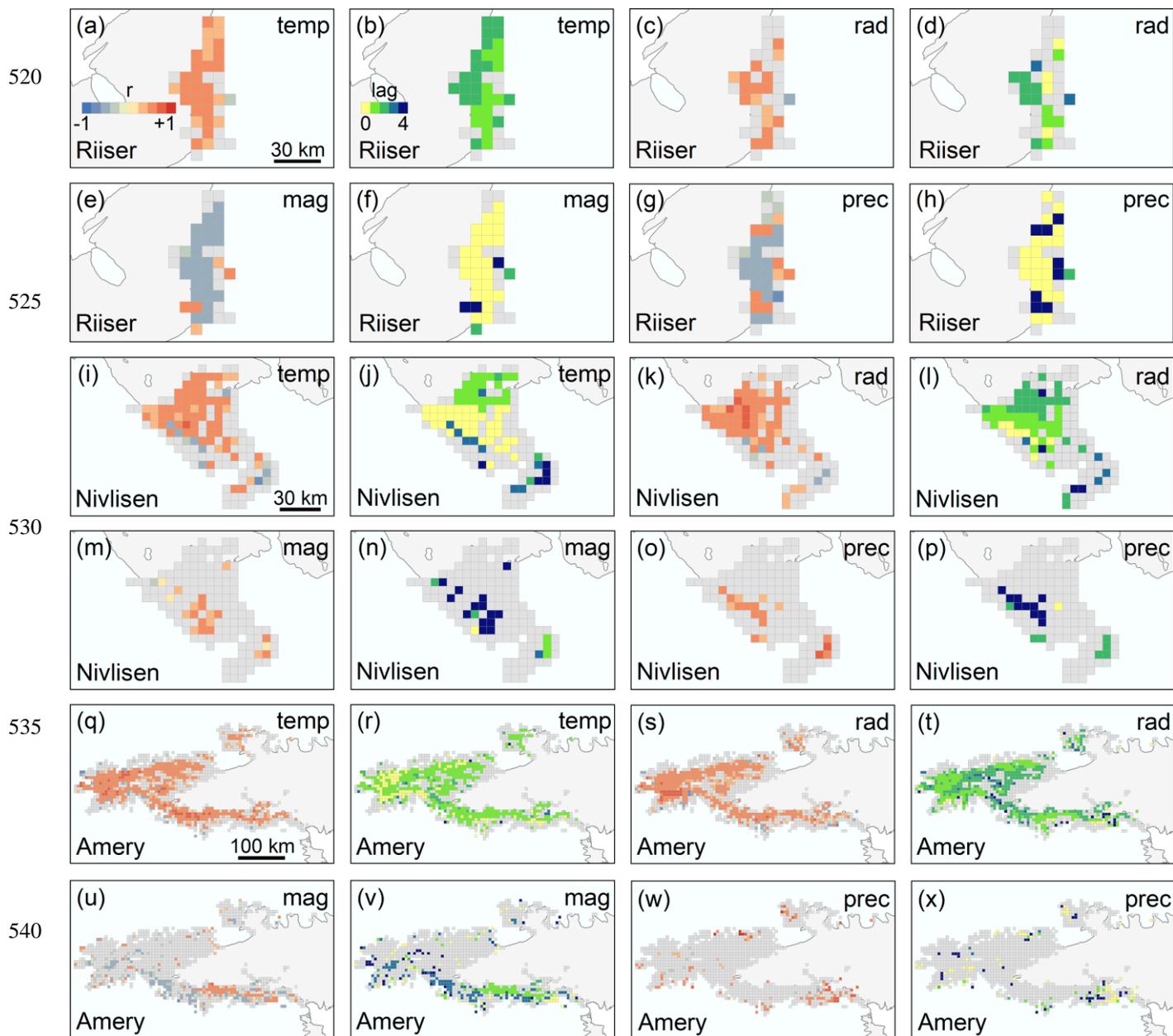
Figure 8 Pixel-based Pearson correlations (r) (a,c,e,g,i,k,m,o,q,s,u,w) and corresponding temporal lags (b,d,f,h,j,l,n,p,r,t,v,x) between fractional lake extents and climate variables air temperature (temp), solar radiation (rad), wind magnitude (mag) and precipitation (prec) over the EAIS ice shelves Riiser-Larsen (a-h), Nivlisen (i-p) and Amery (q-x). Pixels with $p > 0.05$ are masked.
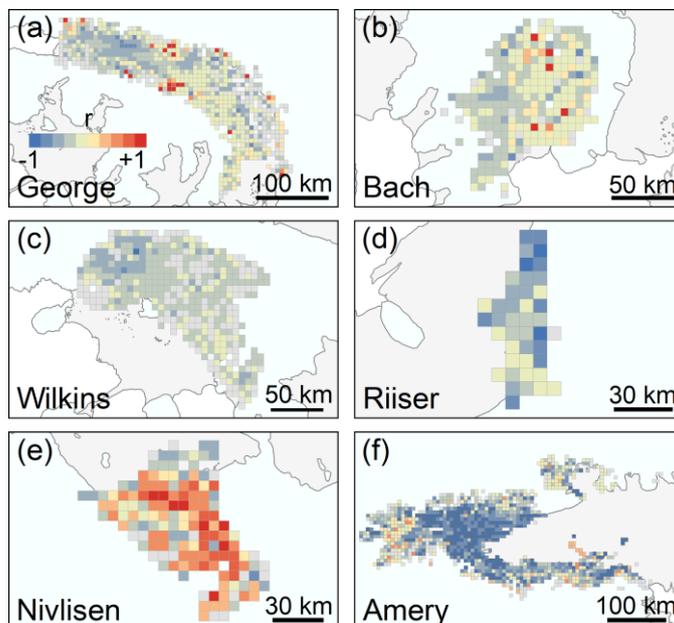
Figure 9 Pixel-based correlations (r) between January fractional lake extents and previous year precipitation over George VI, Bach, Wilkins, Riiser-Larsen, Nivlisen and Amery Ice Shelf. Due to the low number of observations, also correlations with p>0.05 are shown.

5 Discussion

5.1 Environmental controls on supraglacial lake extent dynamics in 2015-2021

5.1.1 Antarctic Peninsula ice shelves

Over API ice shelves, we found a largely coherent inter-annual and intra-annual evolution of lakes with melting seasons 2019-2020 and 2020-2021 being characterised by particularly strong, anomalous high surface ponding during the second half of January and below normal lake extents during most of melting seasons 2015-2018 as well as in late 2020-2021 (Fig. 3a-c, Fig. 4a-c). Cross-correlation analysis demonstrates a time-lagged relationship between supraglacial lake formation and air temperature, also considering temperature extremes (Fig. 6, Fig. 7a,b,i,j,q,r). Highest cross-correlation was found at lag 1 particularly in regions where supraglacial lakes form during high melt years and at lag 0 where lakes form during low melt years closer to the grounding line and rock (Fig. 5a-f, Fig. 7b,j,r). On the one hand, this indicates that meltwater ponding is initiated directly after temperature rises particularly in regions where meltwater accumulation is promoted, e.g., through melt-albedo feedbacks near blue ice or rock outcrop, as present in the vicinity of Wilkins and George VI Ice Shelf (Fig. 1, Fig. 5a,e), while lake formation furthest from regions with albedo-lowering effects occurs at slower time scales. On the other hand, also meltwater transport across the ice shelves later in the melting season can be attributed to higher lags downstream of the grounding lines. Connected drainage systems are in fact visible in the Sentinel-2 image extracts of January 2020 over George VI and Bach Ice Shelf (Fig. 2a-b). Moreover, the observed correlation pattern reveals anomalous high or low lake extents to result from anomalous high or low air temperatures (Fig. 6b). Lag 0 correlation of anomalies of maximum air temperature over

Bach and Wilkins Ice Shelf further points towards a faster response of melting and lake ponding to temperature extremes. These results are well in line with the analysis in Banwell et al. (2021) suggesting anomalous high meltwater ponding in 2019-2020 over George VI Ice Shelf to result from sustained air temperatures ≥0°C. Also, the influence of a strong positive Indian Ocean Dipole (IOD) in 2019 (BOM, 2021) might have contributed to increased air temperatures as well as an early onset of 2019-2020 ponding over George VI Ice Shelf, as suggested for 2020 melting over Larsen C (Bevan et al., 2020). The intensity of IOD can be represented via the Dipole Mode Index (DMI), a measure for the east to west sea surface temperature gradient across the tropical Indian Ocean (see Fig. 10). With DMI returning to neutral to negative values in 2020 (see Fig. 10) (BOM, 2021), other drivers are yet suggested to have caused anomalous high air temperatures and melt during the recent 2020-2021 melting season (see below). Governing the amount of energy available for melt, air temperature was also found to drive lake occurrence on Langhovde Glacier (Langley et al., 2016), EAIS, and could explain the rapid onset of API lake formation within a few weeks (Kingslake et al., 2015; Langley et al., 2016).

Over George VI Ice Shelf, solar radiation was found to exhibit a positive relationship with supraglacial lake occurrence particularly in regions where lakes cluster during high melt years at lags 0-2 (Fig. 5a-b, Fig. 7c-d). In parts, this pattern is visible over regions of high annual lake recurrence on Bach Ice Shelf (Fig. 5c-d, Fig. 7k-l) while the spatial correlation pattern over Wilkins Ice Shelf was heterogeneous. This points towards the amount of incoming solar radiation being an equally important driver for supraglacial lake formation on API ice shelves. Similar conclusions were drawn by Laffin et al. (2021) proposing that enhanced solar radiation is a main driver for foehn-induced melting on Bach and George VI Ice Shelf. In turn, correlation with anomalies of solar radiation over Wilkins Ice Shelf returned a significant negative link at lag 1 and could indicate anomalous supraglacial lake formation to result from enhanced longwave radiation, e.g., due to cloud cover and thus, the higher importance of effects such as sensible heat transport, as suggested in Laffin et al. (2021) and discussed in Banwell et al. (2021). As correlations over Wilkins Ice Shelf were rather heterogeneous overall, the detected pattern could also reflect spurious correlation. Spurious correlation is the result of linear correlations not providing conclusive evidence for causal links. One reason for spurious correlation could be the size of the AOI where numerous pixels show an overall low lake coverage (Fig. 5e) with a potentially varying microclimate. However, weak negative lag 0-1 correlation was also found for George VI and Bach Ice Shelf (Table S2) mostly reflecting an anomalous low availability of incoming solar radiation during the last two melting seasons (Fig. S4c-d). Despite the link between enhanced solar radiation and increased supraglacial lake occurrence over API ice shelves, our results indicate that also an anomalous low availability of solar radiation with respect to previous years can be a weak driver for increased meltwater ponding, e.g., due to enhanced longwave radiation.

Furthermore, cross-correlation of supraglacial lake extents over Wilkins Ice Shelf with anomalies of wind direction (Fig. 6b) as well as pixel-based analysis point towards the existence of a significant negative link at lag 1 (Fig. 7u). Analysing the corresponding time series in more detail, negative correlations seem to be caused by predominant occurrence of north(-easterly) winds preceding recent increased lake ponding (Fig. S4) with most other years characterised by (north-)easterly or north-westerly wind direction. In contrast, positive correlations were visible, e.g., for regions upstream of the grounding line reflecting short-lived shifts to north-westerly winds preceding periods of high lake formation. Shifts in wind direction towards

both, more frequent north(-easterly) or north-westerly winds are also visible in form of negative and positive correlations along the western and eastern grounding lines of George VI and Bach Ice Shelf (Fig. 7e,m). On the one hand, the observed correlations could reflect seasonal cycles of wind. On the other hand, wind conditions are a known driver for supraglacial lake

620   occurrence on the API with previous studies reporting of warm air temperatures over George VI Ice Shelf being promoted by sensible heat transport with warm north-westerly and north-easterly winds as well as a shift towards more frequent north-easterlies (Banwell et al., 2021). Moreover, foehn winds are known to influence surface melting on the north-eastern API (Cape et al., 2015; Datta et al., 2019; Luckman et al., 2014; Turton et al., 2020) and can equally be observed on the western API with (north-)easterly prevailing wind direction (Laffin et al., 2021). This suggests the occurrence of both, foehn conditions

625   and sensible heat transport on the API. Apart from the local topography, foehn winds could explain the clustering of lakes near the grounding lines, where foehn wind influence is assumed to be highest (Lenaerts et al., 2017). As mentioned, also the influence of a positive IOD in 2019 (BOM, 2021) might have contributed to predominant northerly winds in 2019-2020.

Despite ERA5-Land snowmelt data potentially underestimating melt in regions of complex topography (Arthur et al., 2020a), statistical analysis returned positive correlations for both, analysis of spatial averages and anomalies over Bach and

630   Wilkins as well as pixel-based investigation over all three ice shelves (Fig. 7g,o,w). As expected, correlations were highest for time lags 0-1 (Fig. 7h,p,x) with their spatial pattern mostly reflecting the annual recurrence of lakes (Fig. 5a-f). This highlights a link with melt events potentially reflecting short-lived foehn influence (Cape et al., 2015; Turton et al., 2020).

In addition, correlation analysis revealed lake coverage to be peaking in years with previous year low precipitation (Table 1, Fig. 9a-c), reflected in strong negative correlations over regions covered by lakes during high melt years (e.g., Fig. 5a). This

635   highlights supraglacial lake formation to be promoted over more compact, air-depleted firn while fresh snow dampens lake evolution allowing the percolation of meltwater into the low-density firn layer before it can accumulate on the surface (Kuipers Munneke et al., 2014; Lenaerts et al., 2017; Stokes et al., 2019). In fact, the combination of increased API melting in 2019-2020 and low precipitation in 2020 might have led to increased firn air depletion potentially contributing to facilitated melt in 2020-2021. Similarly, low precipitation in 2017 and 2019 likely contributed to enhanced melting in 2017-2018 and 2019-2020,

640   respectively. Correlations with previous year precipitation thus reflect the dependence of meltwater ponding on the FAC, shown to influence lake formation also on Shackleton and Larsen B Ice Shelf (Arthur et al., 2020b; Leeson et al., 2020).

For investigation of large-scale climatic drivers, annual SAM was correlated with January lake extent anomalies. Our results imply a negative relationship for all investigated API ice shelves (Table 1), mostly due to occurrence of a negative SAM year in 2019 (Fig. 10) coincident with enhanced melting in 2019-2020 (Fig. 4a-c). Although the detected relationship

645   seems counterintuitive because negative SAM years usually lead to cold conditions on the API, the mentioned study by Bevan et al. (2020) suggests teleconnections between the tropics and high latitudes in 2019 to be responsible for the observed 2019-2020 melt and negative SAM. In detail, teleconnections caused unusual perturbations of Southern Hemisphere atmospheric flow as well as sudden stratospheric warming (SSW) thus, SAM to be negative and the ongoing positive IOD (Fig. 10) to bring warm air to the API via northerly winds. This overarching driver is well in line with our observations as well as correlations

650   with air temperature and wind. For the recent 2020-2021 melting season, other overarching drivers including SAM returning

to positive values (Fig. 10) as well as modified pressure conditions in the Amundsen Sea Low (ASL) (NSIDC, 2021) are believed to have contributed to high and low lake extents during the early and late 2020-2021 melting season, respectively.
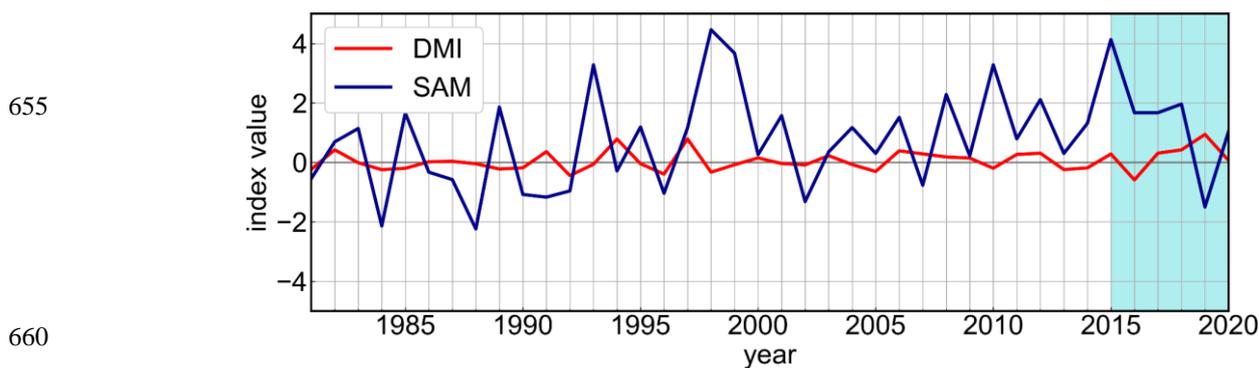
Figure 10 Annual observations of Southern Annular Mode (SAM) and Dipole Mode Index (DMI) between 1981 and 2020. Years 2015-2020 are shaded in turquoise representing our study period. SAM data are from Marshall (2018) and DMI data are available at https://stateoftheocean.osmc.noaa.gov/sur/ind/dmi.php (last accessed 29 June 2021).

Besides, the local topographical setting exerts strong control on supraglacial lake distribution on the API. Over George VI Ice Shelf, meltwater accumulates in latitudinal flow stripes controlled by ice inflow from Palmer Land as well as the prevailing compressive flow regime (see Sect. 2, Fig. 2a, Fig. 5a). Additionally, lake ponding on George VI, Bach and Wilkins Ice Shelf is dictated by the local ice topography with lakes clustering at low elevations and surface slopes (Fig. 2b-c, Fig. 5c,e) being favourable to surface ponding (Arthur et al., 2020a). Likewise, surface depressions on grounded ice control lake formation over all three regions, reflected in a higher recurrence of lakes near the grounding zone. Another factor that could have influenced the spatial distribution of lakes on API ice shelves is the refreezing of lakes in firn pore space causing a modified ice surface topography to affect ponding in the following year (Spergel et al., 2021).

Overall, our results indicate that the complex interplay of lag 0-1 average and maximum air temperature, lag 0-1 snowmelt, lag 0-2 solar radiation as well as wind conditions is among the main controlling factors for 2015-2021 meltwater ponding over the investigated API ice shelves. In particular, variability of climate drivers seems to be linked to supraglacial lake formation below or above average given the high correlation of anomalies. Furthermore, large-scale atmospheric drivers and teleconnections including SAM, IOD and ASL were found to be important to consider for better evaluation of detected drivers. Despite the spatial proximity and similar temporal evolution of lakes on API ice shelves, also the local glaciological and microclimatic setting such as melt-albedo feedbacks, sensible heat exchange or the ice shelf geometry were found to play an important role for supraglacial lake evolution. Likewise, long-term precipitation conditions determine the FAC, found to be a primary control for extensive meltwater ponding on the investigated API ice shelves.

5.1.2 East Antarctic ice shelves

Over EAIS ice shelves, supraglacial lake dynamics were far more variable with frequent supraglacial lake occurrence in 2015-2020 and below average lake occurrence in 2020-2021. Cross-correlation analysis with average air temperature indicates

that supraglacial lake formation on all three ice shelves is driven by temperature at lags 0-2 (Fig. 6a, Fig. 8a,b,i,j,q,r). Also,
high correlation with maximum air temperature over Nivlisen and Amery Ice Shelf indicates supraglacial lake formation to be
facilitated during temperature extremes and correlation of anomalies (Fig. 6b) points towards air temperature controlling
anomalous meltwater ponding on Riiser-Larsen and Nivlisen Ice Shelf. While the detected lag 4 cross-correlation over Amery
Ice Shelf (Fig. 6b) is likely spurious, weak positive lag 1 cross-correlation was found for anomalies of average and maximum
air temperature as well (Table S2). The spatial pattern of temperature time lags (Fig. 8b,j,r) revealed larger lags for regions
where lakes are spreading onto the ice shelves during years of high meltwater ponding and lower lags close to and upstream
of the grounding lines. This likely reflects the temporal evolution of drainage systems through lateral meltwater transport
across the ice shelves (Dell et al., 2020; Spergel et al., 2021), as visible in Fig. 2d-f and Fig. 5g-l, or a longer response time to
air temperature particularly in regions where the local glaciological setting does not promote supraglacial lake formation
through melt-albedo feedbacks. Similarly, air temperature was found to be a primary control for supraglacial lake formation
in 2016-2017 over Nivlisen Ice Shelf (Dell et al., 2020) and on Langhovde Glacier, EAIS (Langley et al., 2016).

Furthermore, cross-correlation with solar radiation returned highest positive relationships at lag 2 over all three ice shelves
(Fig. 6, Fig. 8c,d,k,l,s,t). As above, time lags were highest where lakes expanded furthest onto the ice shelves during years of
high lake coverage, likely reflecting similar effects as described for air temperature. Considering correlation of anomalies,
increased solar radiation seems to control anomalous high meltwater ponding particularly on Riiser-Larsen and Amery Ice
Shelf. Similarly, the availability of incoming solar radiation was shown to contribute to enhanced melting over Roi Baudouin
Ice Shelf, EAIS, where katabatic wind-driven blue ice and firn exposure initiated albedo lowering and enhanced absorption of
solar radiation (Lenaerts et al., 2017). Given the widespread distribution of blue ice near Amery, Riiser-Larsen and Nivlisen
Ice Shelf (Fig. 1d-f, Fig. 2d, Fig. 5i,k), such feedback mechanisms likely occur over the investigated ice shelves. Together
with topographical conditions, melt-albedo feedbacks near rock and blue ice could also explain annual lake clustering near
grounding lines as well as the detected lower lags near the grounding zones (Fig. 8d,l,t).

The observed negative relationship with precipitation conditions over Riiser-Larsen Ice Shelf again highlights that
supraglacial lake formation is controlled by FAC (Fig. 6, Fig. 8g-h). Over Nivlisen and Amery Ice Shelf, no significant
relationship was detected considering both, spatial averages and pixel-based analysis (Fig. 6, Fig. 8o,w). Yet, we found weak
negative correlation (p>0.05) with spatial averages and anomalies over both ice shelves (Table S1, Table S2). This could
indicate that the absence of short-term precipitation is a weak driver for supraglacial lake formation. However, it could also
highlight the higher importance of long-term precipitation effects or of other drivers. In this context, correlation analysis with
previous year precipitation revealed significant negative relationships over Riiser-Larsen and particularly Amery Ice Shelf
(Table 1, Fig. 9d,f) implying that both, a lack of short- and long-term precipitation support high meltwater ponding through a
reduced FAC. Most notably, we found a strong link between 2016-2017 and 2018-2019 high meltwater ponding and previous
year low precipitation over Amery Ice Shelf. In contrast, correlation with previous year precipitation over Nivlisen Ice Shelf
showed a mostly positive, heterogeneous correlation pattern implying the higher importance of other drivers (Fig. 9e).

Moreover, we note supraglacial lake formation on Riiser-Larsen Ice Shelf to be dictated by prevailing low wind speeds following periods of anomalous high wind speeds (Fig. 6, Fig. 8e). In parts, negative correlation is apparent along the south-east grounding line of Amery Ice Shelf (Fig. 8u) while contrasting patterns can be observed along the north-east grounding

720 line and over Nivlisen Ice Shelf (Fig. 8m). For the latter, also weak positive lag 1 cross-correlation with anomalies was found (Table S2). Besides, lag 0-1 wind direction appears to be an important driver for meltwater ponding on Riiser-Larsen and Nivlisen Ice Shelf (Fig. 6a, Fig. S3). Following the analysis of corresponding time series (Fig. S5a-b), short-lived shifts in wind direction from north-easterly to (south-)easterly winds were revealed to be linked to anomalous high lake formation over Riiser-Larsen Ice Shelf. Over Nivlisen Ice Shelf, shifts in wind direction from south-easterly winds towards more (south-

725)easterly winds preceding high supraglacial lake coverage can be attributed to the observed correlations, also reflected in a weak negative lag 1 cross-correlation with anomalies (Fig. S5c-d, Table S2). Besides, analysis of spatial averages and anomalies specified a weak negative lag 1 relationship with wind direction over Amery Ice Shelf (Fig. S5e-f, Table S1, Table S2). Over Amery, the observed lag indicates lakes to be peaking following shifts from south-westerly to southerly winds (Fig. S5e-f). Considering the detected correlation pattern over Riiser-Larsen, we suggest that strong north-easterly winds preceding

730 lake formation together with episodes of low speed (south-)easterly winds during meltwater ponding drive melting, e.g., through katabatic wind forcing. Similarly, anomalous strong (south-)easterly katabatic winds preceding lake formation are suggested to drive surface melting on Nivlisen Ice Shelf also by preserving the nearby blue ice region near Wohlthat mountains (Fig. 1) (Horwath et al., 2006). In fact, easterly katabatic winds warm adiabatically through vertical mixing and can lead to the exposure of albedo-lowering blue ice and firn through wind scouring further enhancing surface melt (Lenaerts et al., 2017).The

735 spatial correlation pattern over Amery Ice Shelf is twofold. Along the north-east grounding line, supraglacial lakes peak shortly after occurrence of high-speed (south-)easterly winds likely reflecting the influence of katabatic winds flowing onto the ice shelf via the adjacent eastern plateau (e.g., Stokes et al., 2019). In contrast, supraglacial lakes in the south of Amery Ice Shelf peak during low-speed winds from south(-east) or south-(west) following high-speed southerly winds. This indicates that katabatic winds drive melting in agreement with the local topography determining the direction of wind inflow but also through

740 melt-albedo feedbacks explaining the predominant occurrence of correlations along the grounding line of Amery Ice Shelf (Fig. 1f, Fig. 5k-l). Wind conditions are a known driver for supraglacial lake formation in East Antarctica with katabatic winds driving melting on Shackleton or Roi Baudouin Ice Shelf (Arthur et al., 2020b; Lenaerts et al., 2017).

Besides, significant cross-correlation with lag 1 snowmelt over Riiser-Larsen and Amery Ice Shelf suggests direct links with short-lived modelled snowmelt events (Fig. 6, Fig. S3). At the same time, the observed negative correlation over Nivlisen

745 Ice Shelf is likely spurious, potentially due to the temporal lag of 4 being rather high. In fact, weak positive lag 0 correlations are apparent for Nivlisen Ice Shelf as well (Table S1, Table S2, Fig. S3). Correlation with modelled snowmelt could reflect localised katabatic wind-induced peaks in melting, as suggested for Shackleton Ice Shelf (Arthur et al., 2020b).

Further, correlation with SAM returned a negative relationship for Riiser-Larsen Ice Shelf (Table 1). This could point towards Southern Hemisphere atmospheric modes including IOD similarly affecting western East Antarctica, e.g., due to the

750 spatial proximity to the Weddell Sea. In fact, January 2020 lake extents were far above average over Riiser-Larsen in agreement

with a positive IOD/DMI and negative SAM (Fig. 10). Correlations with SAM over Nivlisen and Amery Ice Shelf were weak positive (Table 1) potentially reflecting the opposite climate effects SAM can have on the API and EAIS (Kwok and Comiso, 2002; Wachter et al., 2020). As mentioned, also the influence of an atypical ASL driving below average temperature and melt along large parts of East Antarctica in 2020-2021 (NSIDC, 2021) has to be considered most likely explaining below average

755   lake extents over EAIS ice shelves (Fig. 4d-f) as well as corresponding positive correlations with air temperature.

Table 2 Summary of suggested controls on 2015-2021 meltwater ponding across six Antarctic ice shelves. The results present a summary of pixel-based and spatially averaged correlations, also considering weak correlations and neglecting spurious results where appropriate. Positive and negative signs indicate positive and negative relationships, respectively. Signs '+/-' and '/' denote the coexistence of positive and negative links as well as no observed links, respectively. The strength or lag of correlations is not shown.

Scale	Variable	Antarctic Peninsula ice shelves			East Antarctic ice shelves		
		George VI	Bach	Wilkins	Riiser-Larsen	Nivlisen	Amery
Local controls	Melt-albedo feedbacks	+	/	+	+	+	+
	Elevation/slope	-	-	-	-	-	-
	Ice surface morphology*	+	+	+	+	+	+
	Firn air content	-	-	-	-	/	-
Regional climate	Air temperature	+	+	+	+	+	+
	Max. air temperature	+	+	+	/	+	+
	Solar radiation	+/-	+/-	-	+	+	+
	Short-term precipitation	/	/	/	-	-	-
	Wind speed	/	/	/	-	+	+/-
	Wind direction	+/-	+/-	+/-	+	-	-
	Snowmelt	+	+	+	+	+	+
Atmospheric modes	SAM	-	-	-	-	+	+
	DMI/IOD and SWW	+	+	+	+	**	**
	Intense ASL	-	-	-	-	-	-

760   *the positive sign refers to the existence of a link without directional component **not investigated but likely weak negative

The high recurrence of lakes on EAIS ice shelves (Fig. 5g-l) reflects lakes reforming in the same location each year thus, the high importance of the ice surface topography (Arthur et al., 2020a; Echelmeyer et al., 1991; Langley et al., 2016). Over Riiser-Larsen and particularly Nivlisen Ice Shelf, elongated meltwater bodies were found to reoccupy the same ice shelf surface depressions (Fig. 5h-j) meaning that the local topography exerts strong control on the inter-annual distribution of meltwater.

765   Consistent results were found for melting season 2016-2017 over Nivlisen Ice Shelf (Dell et al., 2020). Lake ponding over Amery Ice Shelf seems to be dictated by both, local surface depressions on grounded ice as well as longitudinal flow stripes migrating with ice flow on floating ice (Fig. 2f, Fig. 5k-l) (Glasser and Gudmundsson, 2012; Spergel et al., 2021). Furthermore, also the refreezing of lakes in firn pore space could have influenced lake ponding through a modification of the ice surface topography as well as firn air depletion (Kuipers Munneke et al., 2014; Spergel et al., 2021).

770   To summarise, we find slightly varying drivers for supraglacial lake formation on each investigated ice shelf with Riiser-
Larsen being influenced by most investigated parameters, Nivlisen by air temperature, solar radiation, wind as well as local
controls and Amery by air temperature, solar radiation, wind, snowmelt, local controls and particularly the FAC. In addition,
large-scale climatic drivers and teleconnections including SAM, IOD or ASL are linked to fluctuations in climate and lake
extents. Table 2 provides a summary of all detected drivers considering correlation with spatial averages and anomalies as well
775   as pixel-based analysis. Where appropriate, detected weak correlations are included and potential spurious correlations are
neglected. Yet, it has to be noted that the interplay of climate variables might have led to non-linear relations not captured in
our correlations and the comparatively low number of observations to correlations being flagged as insignificant despite the
existence of causal links. Besides, more detailed investigation of teleconnections would require additional atmospheric indices.

5.2 Potential implications for future ice shelf stability

780   Future atmospheric warming is expected to enhance meltwater production and ponding on Antarctic ice shelves (Bell et al.,
2018; Kingslake et al., 2017; Trusel et al., 2015). Extensive surface ponding threatens ice shelf stability due to variations in
stress causing flexure (Banwell et al., 2019) and ultimately vertical fracturing and ice shelf collapse effectively reducing ice
shelf buttressing (Banwell and Macayeal, 2015; Dunmire et al., 2020; Leeson et al., 2020; Rott et al., 2018; Scambos et al.,
2004). Ice shelves that are vulnerable to hydrofracturing are widespread around Antarctica (Alley et al., 2018; Lai et al., 2020)
785   particularly when they are pre-weakened by fractures and crevasses (Lhermitte et al., 2020) or firn air depletion (Kuipers
Munneke et al., 2014; Lenaerts et al., 2017; Spergel et al., 2021). Lateral meltwater transport across ice shelves delivers
meltwater to regions with only little or no surface melt effectively reducing the FAC and making them more vulnerable to
hydrofracture (Dell et al., 2020). This is particularly prevalent in the absence of efficient drainage system transporting
meltwater to the ocean (Bell et al., 2017). Given repeated meltwater ponding and drainage across the investigated ice shelves
790   during the last 5-6 melting seasons (Fig. 5), future ice shelf destabilisation could be imminent considering the classification of
respective ice shelf areas as potentially vulnerable to hydrofracture (Lai et al., 2020). This particularly applies to ice shelves
on the API, where exceptional meltwater ponding during the last two melting seasons likely contributed to further firn air
depletion, as suggested for Larsen C (Bevan et al., 2020). Future enhanced precipitation due to an enhanced moisture holding
capacity of warmer air may partly compensate this (Bell et al., 2018; Bengtsson et al., 2011; Krinner et al., 2007; Lenaerts et
795   al., 2016) even though additional research is required for better evaluation of all factors. Similarly, increasingly positive IODs
under high emission scenarios may counteract API warming in the absence of perturbations such as SSW (Bevan et al., 2020).

6   Conclusions

This study presents the first intra-annual and inter-annual investigation of Antarctic surface hydrology across six major
Antarctic ice shelves employing state-of-the-art machine learning on spaceborne observations from Sentinel-1 SAR and optical
800   Sentinel-2. We derive fused classification products at unprecedented 10 m spatial resolution and bi-weekly temporal scale to
map Antarctic surface hydrological features in 2015-2021. In this context, the integration of SAR data enabled the delineation

of also buried lakes providing a more complete mapping record than single-sensor products. For the investigated Antarctic Peninsula ice shelves, our results reveal anomalous low supraglacial lake coverage during most of melting seasons 2015-2018 and anomalous high lake coverage during summers 2019-2020 and 2020-2021. Peak lake coverage reached 805 km² in late

805   January 2020 over George VI Ice Shelf. Over East Antarctic ice shelves, supraglacial lake extents fluctuated more substantially with most of melting seasons 2016-2020 being characterised by above average lake coverage and melting season 2020-2021 by record low lake coverage. On the EAIS, highest lake coverage was found on Amery Ice Shelf peaking at 1373 km² in early January 2019. Further, we observe lateral meltwater transport in surface drainage systems to occur over both, Antarctic Peninsula and East Antarctic ice shelves with potential implications for future ice shelf stability.

810   To establish a link between intra-annual supraglacial lake extent dynamics in 2015-2021 and potential environmental drivers, we employ multi-temporal linear correlation analysis at different time lags using spatio-temporal observations of ERA5-Land climate reanalysis data. Moreover, inter-annual observations of supraglacial lake extents are used to investigate the influence of large-scale atmospheric modes as well as of the local glaciological setting including the state of the firn layer. Results of the statistical analysis with spatial averages and anomalies as well as with pixel-based values return a strong coupling

815   between temporal fluctuations in Antarctic Peninsula supraglacial lake extents and lag 0-1 average and maximum air temperature, lag 0-1 snowmelt, lag 0-2 solar radiation as well as wind direction with lake extents below or above average being linked to anomalies of climate variables. In addition, correlations with annual Southern Annular Mode revealed significant relationships with large-scale atmospheric drivers and investigation of previous year precipitation implied the strong influence of reduced snow conditions promoting supraglacial lake formation through a reduction of the firn air content. Also, pixel-

820   based analysis revealed a faster response time of lake evolution to climate drivers in regions where surface features such as blue ice or rock initiate melt-albedo feedbacks. Over East Antarctic ice shelves, we found varying patterns for each ice shelf. For Riiser-Larsen, statistical correlation analysis implied a coupling between supraglacial lake extent dynamics and lag 1-2 air temperature, lag 0-2 solar radiation, lag 0 wind conditions, lag 0 precipitation conditions and lag 1 snowmelt. On the other hand, supraglacial lake extent dynamics over Nivlisen Ice Shelf are linked to lag 0-1 air temperature, lag 0-2 solar radiation,

825   lag 1 wind conditions as well as lag 0-1 snowmelt and statistical analysis over Amery Ice Shelf points toward a coupling with lag 0-1 air temperature, lag 1-4 solar radiation, lag 1 snowmelt and wind conditions. Similar as for API ice shelves, anomalous surface ponding was linked to anomalies of detected climate drivers. At the same time, the influence of Southern Hemisphere atmospheric modes and the local glaciological setting including the ice shelf geometry and elevation as well as melt-albedo feedbacks are found to exert strong control on supraglacial lake formation. Moreover, the influence of a reduced firn air content

830   over Riiser-Larsen and particularly Amery Ice Shelf was related to above normal supraglacial lake formation.

To summarise, our findings provide important insight into present-day Antarctic surface hydrology and associated drivers and could be particularly useful for an improved representation of meltwater transport across Antarctic ice shelves in modelling efforts (Buzzard et al., 2018). Specifically, the results of this study underline the complex interplay of climate variables at different time lags and the local glaciological setting to be influencing supraglacial lake formation both, spatially and

835   temporally. Furthermore, the value of ERA5-Land and Copernicus Sentinel data were highlighted with the growing archive of

satellite data enabling more detailed analyses on supraglacial lake dynamics in the future. In particular, future work will focus on the generation of circum-Antarctic supraglacial lake extent mapping products, to be made available via the EOC GeoService of the German Aerospace Center, the expansion of statistical analyses to continental scale as well as the application of advanced causal analysis techniques. Once available, the integration of higher resolution model outputs from RACMO (Regional
840 Atmospheric Climate Model) (van Wessem et al., 2018) as well as more detailed investigation of teleconnections with additional atmospheric indices will be considered to better constrain climate drivers.

Data availability

The Supplement provides results from statistical correlation of fractional supraglacial lake extents and bi-weekly spatial averages (Table S1) and anomalies (Table S2) over the six investigated Antarctic ice shelves. Moreover, supplementary Fig.
845 S1 provides information on the share of data originating from Sentinel-1 and Sentinel-2 in bi-weekly classifications. Fig. S2 and Fig. S3 provide pixel-based correlation results for all variables not shown in Fig. 7 and Fig. 8. Fig. S4 and Fig. S5 show auxiliary plots on spatially averaged wind direction and lake extents for Wilkins, Riiser-Larsen, Nivlisen and Amery Ice Shelf to complement the conclusions made in Sect. 5. Fig. S4 also shows results for lag 1 solar radiation.

The outline of the Antarctic ice sheets is taken from http://imbie.org/imbie-2016/drainage-basins/ (IMBIE, 2016) and
850 coastline and grounding line data are available at https://nsidc.org/data/NSIDC-0709/versions/2# (Mouginot et al., 2017; Rignot et al., 2013). The Landsat Image Mosaic of Antarctica (LIMA) was downloaded from https://lima.usgs.gov/fullcontinent.php (Bindschadler et al., 2008) and the gap-filled 200 m Reference Elevation Model of Antarctica is from https://data.pgc.umn.edu/elev/dem/setsm/REMA/ (Howat et al., 2019). The TanDEM-X PolarDEM (Wessel et al., 2021) (https://download.geoservice.dlr.de/TDM_POLARDEM90/ANTARCTICA/) and 2018 Antarctic coastline
855 (Baumhoer et al., 2021) (https://download.geoservice.dlr.de/icelines/files/) are provided via the EOC GeoService of the German Aerospace Center. Southern Annular Mode index data (Marshall, 2018, 2003) can be accessed at https://legacy.bas.ac.uk/met/gjma/sam.html and Dipole Mode Index data are provided by the NOAA/ESRL, Boulder, Colorado, USA, from their Web site at https://stateoftheocean.osmc.noaa.gov/sur/ind/dmi.php. ERA5-Land reanalysis data from Munoz Sabater (2019) were downloaded from the Copernicus Climate Change Service (C3S) Climate Data Store
860 (https://cds.climate.copernicus.eu). The results contain modified Copernicus Climate Change Service information 2021. Neither the European Commission nor ECMWF is responsible for any use that may be made of the Copernicus information or data it contains.

Author Contributions

MD designed the study, conducted the analysis, and wrote the original draft of the manuscript. CK and AD assisted in the
865 study design. MD, CK and AD contributed to the discussion of the results and were involved in editing the manuscript.

Competing interests

The authors declare that they have no conflicts of interest.

Acknowledgements

We thank the Copernicus Climate Change Service (C3S) Climate Data Store for providing ERA5-Land reanalysis data.
870 Moreover, we thank the European Union Copernicus programme for providing Sentinel-1 and Sentinel-2 data. Matthias
Hofmann and Andreas Jahnke, DLR, are acknowledged for their support with Sentinel data access and Julian Zeidler and
Soner Uereyen, DLR, are acknowledged for IT support and proof-reading. Authors also acknowledge Gareth Marshall for
granting open access to the Southern Annular Mode index and NOAA/ESRL for Dipole Mode Index data.

References

875

Alley, K. E., Scambos, T. A., Miller, J. Z., Long, D. G., and MacFerrin, M.: Quantifying vulnerability of Antarctic ice shelves
    to hydrofracture using microwave scattering properties, Remote Sens. Environ., 210, 297–306,
    https://doi.org/10.1016/j.rse.2018.03.025, 2018.
Arthur, J. F., Stokes, C. R., Jamieson, S. S. R., Carr, J. R., and Leeson, A. A.: Distribution and seasonal evolution of
880   supraglacial lakes on Shackleton Ice Shelf, East Antarctica, The Cryosphere, 14, 4103–4120,
    https://doi.org/10.5194/tc-14-4103-2020, 2020a.
Arthur, J. F., Stokes, C. R., Jamieson, S. S. R., Carr, J. R., and Leeson, A. A.: Recent understanding of Antarctic supraglacial
    lakes using satellite remote sensing, Prog. Phys. Geogr., 44, 837–869, https://doi.org/10.1177/0309133320916114,
    2020b.
885 Banwell, A. F. and Macayeal, D. R.: Ice-shelf fracture due to viscoelastic flexure stress induced by fill/drain cycles of
    supraglacial lakes, Antarct. Sci., 27, 587–597, https://doi.org/10.1017/S0954102015000292, 2015.
Banwell, A. F., MacAyeal, D. R., and Sergienko, O. V.: Breakup of the Larsen B Ice Shelf triggered by chain reaction drainage
    of supraglacial lakes, Geophys. Res. Lett., 40, 5872–5876, https://doi.org/10.1002/2013GL057694, 2013.
Banwell, A. F., Willis, I. C., Macdonald, G. J., Goodsell, B., and MacAyeal, D. R.: Direct measurements of ice-shelf flexure
890   caused by surface meltwater ponding and drainage, Nat. Commun., 10, 1–10, https://doi.org/10.1038/s41467-019-
    08522-5, 2019.
Banwell, A. F., Datta, R. T., Dell, R. L., Moussavi, M., Brucker, L., Picard, G., Shuman, C. A., and Stevens, L. A.: The 32-
    year record-high surface melt in 2019/2020 on the northern George VI Ice Shelf, Antarctic Peninsula, The Cryosphere,
    15, 909–925, https://doi.org/10.5194/tc-15-909-2021, 2021.
895 Bartholomew, I., Nienow, P., Mair, D., Hubbard, A., King, M. A., and Sole, A.: Seasonal evolution of subglacial drainage and
    acceleration in a Greenland outlet glacier, Nat. Geosci., 3, 408–411, https://doi.org/10.1038/ngeo863, 2010.
Baumhoer, C. A., Dietz, A. J., Kneisel, C., Paeth, H., and Kuenzer, C.: Environmental drivers of circum-Antarctic glacier and
    ice shelf front retreat over the last two decades, The Cryosphere, 15, 2357–2381, https://doi.org/10.5194/tc-15-2357-
    2021, 2021.
900 Bell, R. E., Chu, W., Kingslake, J., Das, I., Tedesco, M., Tinto, K. J., Zappa, C. J., Frezzotti, M., Boghosian, A., and Lee, W.
    S.: Antarctic ice shelf potentially stabilized by export of meltwater in surface river, Nature, 544, 344–348,
    https://doi.org/10.1038/nature22048, 2017.
Bell, R. E., Banwell, A. F., Trusel, L. D., and Kingslake, J.: Antarctic surface hydrology and impacts on ice-sheet mass balance,
    Nat. Clim. Change, 8, 1044, https://doi.org/10.1038/s41558-018-0326-3, 2018.
905 Bengtsson, L., Koumoutsaris, S., and Hodges, K.: Large-Scale Surface Mass Balance of Ice Sheets from a Comprehensive
    Atmospheric Model, Surv. Geophys., 32, 459, https://doi.org/10.1007/s10712-011-9120-8, 2011.

Berthier, E., Scambos, T. A., and Shuman, C. A.: Mass loss of Larsen B tributary glaciers (Antarctic Peninsula) unabated since 2002, Geophys. Res. Lett., 39, https://doi.org/10.1029/2012GL051755, 2012.

910 Bevan, S., Luckman, A., Hendon, H., and Wang, G.: The 2020 Larsen C Ice Shelf surface melt is a 40-year record high, The Cryosphere, 14, 3551–3564, https://doi.org/10.5194/tc-14-3551-2020, 2020.

Bindschadler, R., Vornberger, P., Fleming, A., Fox, A., Mullins, J., Binnie, D., Paulsen, S. J., Granneman, B., and Gorodetzky, D.: The Landsat Image Mosaic of Antarctica, Remote Sens. Environ., 112, 4214–4226, https://doi.org/10.1016/j.rse.2008.07.006, 2008.

BOM: Climate Driver Update: http://www.bom.gov.au/climate/enso/, last accessed: 22 June 2021, 2021.

915 Buzzard, S., Feltham, D., and Flocco, D.: Modelling the fate of surface melt on the Larsen C Ice Shelf, The Cryosphere, 12, 3565–3575, https://doi.org/10.5194/tc-12-3565-2018, 2018.

Cape, M. R., Vernet, M., Skvarca, P., Marinsek, S., Scambos, T., and Domack, E.: Foehn winds link climate-driven warming to ice shelf evolution in Antarctica, J. Geophys. Res.-Atmos., 120, 11,037-11,057, https://doi.org/10.1002/2015JD023465, 2015.

920 Cook, A. J. and Vaughan, D. G.: Overview of areal changes of the ice shelves on the Antarctic Peninsula over the past 50 years, The Cryosphere, 4, 77–98, https://doi.org/10.5194/tc-4-77-2010, 2010.

Datta, R. T., Tedesco, M., Fettweis, X., Agosta, C., Lhermitte, S., Lenaerts, J. T. M., and Wever, N.: The Effect of Foehn-Induced Surface Melt on Firn Evolution Over the Northeast Antarctic Peninsula, Geophys. Res. Lett., 46, 3822–3831, https://doi.org/10.1029/2018GL080845, 2019.

925 Dell, R., Arnold, N., Willis, I., Banwell, A., Williamson, A., Pritchard, H., and Orr, A.: Lateral meltwater transfer across an Antarctic ice shelf, The Cryosphere, 14, 2313–2330, https://doi.org/10.5194/tc-14-2313-2020, 2020.

Dirscherl, M., Dietz, A. J., Kneisel, C., and Kuenzer, C.: Automated Mapping of Antarctic Supraglacial Lakes Using a Machine Learning Approach, Remote Sens., 12, https://doi.org/10.3390/rs12071203, 2020.

Dirscherl, M., Dietz, A. J., Kneisel, C., and Kuenzer, C.: A Novel Method for Automated Supraglacial Lake Mapping in 930 Antarctica Using Sentinel-1 SAR Imagery and Deep Learning, Remote Sens., 13, 197, https://doi.org/10.3390/rs13020197, 2021.

Dunmire, D., Lenaerts, J. T. M., Banwell, A. F., Wever, N., Shragge, J., Lhermitte, S., Drews, R., Pattyn, F., Hansen, J. S. S., Willis, I. C., Miller, J., and Keenan, E.: Observations of Buried Lake Drainage on the Antarctic Ice Sheet, Geophys. Res. Lett., 47, e2020GL087970, https://doi.org/10.1029/2020GL087970, 2020.

935 Echelmeyer, K., Clarke, T. S., and Harrison, W. D.: Surficial glaciology of Jakobshavns Isbræ, West Greenland: Part I. Surface morphology, J. Glaciol., 37, 368–382, https://doi.org/10.3189/S0022143000005803, 1991.

Foley, K. M., Ferrigno, J. G., Swithinbank, C., Williams, R. S. Jr., and Orndorff, A. L.: Coastal-Change and Glaciological Map of the Amery Ice Shelf Area, Antarctica: 1961—2004, https://doi.org/10.1016/j.jag.2019.01.008, 2013.

Fürst, J. J., Durand, G., Gillet-Chaulet, F., Tavard, L., Rankl, M., Braun, M., and Gagliardini, O.: The safety band of Antarctic 940 ice shelves, Nat. Clim. Change, 6, 479–482, https://doi.org/10.1038/nclimate2912, 2016.

Gardner, A. S., Moholdt, G., Scambos, T., Fahnstock, M., Ligtenberg, S., Van den Broeke, M., and Nilsson, J.: Increased West Antarctic and unchanged East Antarctic ice discharge over the last 7 years, The Cryosphere, 12, 521–547, https://doi.org/10.5194/tc-12-521-2018, 2018.

Glasser, N. F. and Gudmundsson, G. H.: Longitudinal surface structures (flowstripes) on Antarctic glaciers, The Cryosphere, 945 6, 383–391, https://doi.org/10.5194/tc-6-383-2012, 2012.

Gossart, A., Helsen, S., Lenaerts, J. T. M., Broucke, S. V., Lipzig, N. P. M. van, and Souverijns, N.: An Evaluation of Surface Climatology in State-of-the-Art Reanalyses over the Antarctic Ice Sheet, J. Climate, 32, 6899–6915, https://doi.org/10.1175/JCLI-D-19-0030.1, 2019.

Halberstadt, A. R. W., Gleason, C. J., Moussavi, M. S., Pope, A., Trusel, L. D., and DeConto, R. M.: Antarctic Supraglacial 950 Lake Identification Using Landsat-8 Image Classification, Remote Sens., 12, 1327, https://doi.org/10.3390/rs12081327, 2020.

Hambrey, M. J., Davies, B. J., Glasser, N. F., Holt, T. O., Smellie, J. L., and Carrivick, J. L.: Structure and sedimentology of George VI Ice Shelf, Antarctic Peninsula: implications for ice-sheet dynamics and landform development, J. Geol. Soc., 172, 599–613, https://doi.org/10.1144/jgs2014-134, 2015.

955 Hogg, A. E., Shepherd, A., Cornford, S. L., Briggs, K. H., Gourmelen, N., Graham, J. A., Joughin, I., Mouginot, J., Nagler, T., Payne, A. J., Rignot, E., and Wuite, J.: Increased ice flow in Western Palmer Land linked to ocean melting, Geophys. Res. Lett., 44, 4159–4167, https://doi.org/10.1002/2016GL072110, 2017.

Holt, T., Glasser, N. F., Quincey, D. J., and Siegfried, M. R.: Speedup and fracturing of George VI Ice Shelf, Antarctic Peninsula, The Cryosphere, 7, 797–816, https://doi.org/10.5194/tc-7-797-2013, 2013a.

960 Holt, T., Glasser, N., and Quincey, D.: The structural glaciology of southwest Antarctic Peninsula Ice Shelves (ca. 2010), J. Maps, 9, 523–531, https://doi.org/10.1080/17445647.2013.822836, 2013b.

Horwath, M., Dietrich, R., Baessler, M., Nixdorf, U., Steinhage, D., Fritzsche, D., Damm, V., and Reitmayr, G.: Nivlisen, an Antarctic ice shelf in Dronning Maud Land: geodetic–glaciological results from a combined analysis of ice thickness, ice surface height and ice-flow observations, J. Glaciol., 52, 17–30, https://doi.org/10.3189/172756506781828953, 965 2006.

Howat, I. M., Porter, C., Smith, B. E., Noh, M.-J., and Morin, P.: The Reference Elevation Model of Antarctica, The Cryosphere, 13, 665–674, https://doi.org/10.5194/tc-13-665-2019, 2019.

IMBIE: Antarctica and Greenland Ice Sheet Drainage Basins: http://imbie.org/imbie-2016/drainage-basins/, last accessed: 15 June 2021, 2016.

970 Jiang, H., Yang, Y., Bai, Y., and Wang, H.: Evaluation of the Total, Direct, and Diffuse Solar Radiations From the ERA5 Reanalysis Data in China, IEEE Geosci. Remote Sens. Lett., 17, 47–51, https://doi.org/10.1109/LGRS.2019.2916410, 2020.

Jolly, K.: Machine Learning with scikit-learn Quick Start Guide, Packt Publishing Ltd., Birmingham, UK, 2018.

Kingslake, Ely, J. C., Das, I., and Bell, R. E.: Widespread movement of meltwater onto and across Antarctic ice shelves, 975 Nature, 544, 349–352, https://doi.org/10.1038/nature22049, 2017.

Kingslake, J., Ng, F., and Sole, A.: Modelling channelized surface drainage of supraglacial lakes, J. Glaciol., 61, 185–199, https://doi.org/10.3189/2015JoG14J158, 2015.

Kleiner, T. and Humbert, A.: Numerical simulations of major ice streams in Western Dronning Maud Land, Antarctica, under wet and dry basal conditions, J. Glaciol., 60, 215–232, https://doi.org/10.3189/2014JoG13J006, 2014.

980 Krinner, G., Magand, O., Simmonds, I., Genthon, C., and Dufresne, J.-L.: Simulated Antarctic precipitation and surface mass balance at the end of the twentieth and twenty-first centuries, Clim. Dyn., 28, 215–230, https://doi.org/10.1007/s00382-006-0177-x, 2007.

Kuipers Munneke, P., Ligtenberg, S. R. M., Broeke, M. R. V. D., and Vaughan, D. G.: Firn air depletion as a precursor of Antarctic ice-shelf collapse, J. Glaciol., 60, 205–214, https://doi.org/10.3189/2014JoG13J183, 2014.

985 Kwok, R. and Comiso, J. C.: Spatial patterns of variability in Antarctic surface temperature: Connections to the Southern Hemisphere Annular Mode and the Southern Oscillation, Geophys. Res. Lett., 29, 50-1-50–4, https://doi.org/10.1029/2002GL015415, 2002.

LaBarbera, C. H. and MacAyeal, D. R.: Traveling supraglacial lakes on George VI Ice Shelf, Antarctica, Geophys. Res. Lett., 38, https://doi.org/10.1029/2011GL049970, 2011.

990 Laffin, M. K., Zender, C. S., Singh, S., Wessem, J. M. V., Smeets, C. J. P. P., and Reijmer, C. H.: Climatology and Evolution of the Antarctic Peninsula Föhn Wind-Induced Melt Regime From 1979–2018, Geophys. Res. Lett., 126, e2020JD033682, https://doi.org/10.1029/2020JD033682, 2021.

Lai, C.-Y., Kingslake, J., Wearing, M. G., Chen, P.-H. C., Gentine, P., Li, H., Spergel, J. J., and Wessem, J. M. van: Vulnerability of Antarctica's ice shelves to meltwater-driven fracture, Nature, 584, 574–578, 995 https://doi.org/10.1038/s41586-020-2627-8, 2020.

Langley, E. S., Leeson, A. A., Stokes, C. R., and Jamieson, S. S. R.: Seasonal evolution of supraglacial lakes on an East Antarctic outlet glacier, Geophys. Res. Lett., 43, 8563–8571, https://doi.org/10.1002/2016GL069511, 2016.

Leeson, A. A., Forster, E., Rice, A., Gourmelen, N., and Van Wessem, J. M.: Evolution of supraglacial lakes on the Larsen B ice shelf in the decades before it collapsed, Geophys. Res. Lett., 47, https://doi.org/10.1029/2019GL085591, 2020.

1000 Lenaerts, J. T. M., Vizcaino, M., Fyke, J., van Kampenhout, L., and van den Broeke, M. R.: Present-day and future Antarctic ice sheet climate and surface mass balance in the Community Earth System Model, Clim. Dyn., 47, 1367–1381, https://doi.org/10.1007/s00382-015-2907-4, 2016.

Lenaerts, J. T. M., Lhermitte, S., Drews, R., Ligtenberg, S. R. M., Berger, S., Helm, V., Smeets, C. J. P. P., Broeke, M. R. van den, van de Berg, W. J., van Meijgaard, E., Eijkelboom, M., Eisen, O., and Pattyn, F.: Meltwater produced by wind–

1005   albedo interaction stored in an East Antarctic ice shelf, Nat. Clim. Change, 7, 58–62, https://doi.org/10.1038/nclimate3180, 2017.

Lhermitte, S., Sun, S., Shuman, C., Wouters, B., Pattyn, F., Wuite, J., Berthier, E., and Nagler, T.: Damage accelerates ice shelf instability and mass loss in Amundsen Sea Embayment, PNAS, 117, 24735–24741, https://doi.org/10.1073/pnas.1912890117, 2020.

1010   Louis, J., Debaecker, V., Pflug, B., Main-Knorn, M., Bieniarz, J., Mueller-Wilm, U., Cadau, E., and Gascon, F.: Sentinel-2 Sen2Cor: L2A Processor For Users, in: Proc. Living Planet Symposium 2016, Prague, Czech Republic, 2016.

Luckman, A., Elvidge, A., Jansen, D., Kulessa, B., Munneke, P. K., King, J., and Barrand, N. E.: Surface melt and ponding on Larsen C Ice Shelf and the impact of föhn winds, Antarct. Sci., 26, 625–635, https://doi.org/10.1017/S0954102014000339, 2014.

1015   Marshall, G. J.: Trends in the Southern Annular Mode from Observations and Reanalyses, J. Climate, 16, 4134–4143, https://doi.org/10.1175/1520-0442(2003)016<4134:TITSAM>2.0.CO;2, 2003.

Marshall, G. J.: The Climate Data Guide: Marshall Southern Annular Mode (SAM) Index (Station-based), edited by: National Center for Atmospheric Research Staff, https://climatedataguide.ucar.edu/climate-data/marshall-southern-annular-mode-sam-index-station-based, last accessed: 20 June 2021, 2018.

1020   Meredith, M., Sommerkorn, M., Cassotta, S., Derksen, C., Ekaykin, A., Hollowed, A., Kofinas, G., Mackintosh, A., Melbourne-Thomas, J., Muelbert, M. M. C., Ottersen, G., Pritchard, H., and Schuur, E. A. G.: Polar Regions. In: IPCC Special Report on the Ocean and Cryosphere in a Changing Climate [H.-O. Pörtner, D.C. Roberts, V. Masson-Delmotte, P. Zhai, M. Tignor, E. Poloczanska, K. Mintenbeck, A. Alegría, M. Nicolai, A. Okem, J. Petzold, B. Rama, N.M. Weyer (eds.)]. In press., 2019.

1025   Minchew, B. M., Gudmundsson, G. H., Gardner, A. S., Paolo, F. S., and Fricker, H. A.: Modeling the dynamic response of outlet glaciers to observed ice-shelf thinning in the Bellingshausen Sea Sector, West Antarctica, J. Glaciol., 64, 333–342, https://doi.org/10.1017/jog.2018.24, 2018.

Mouginot, J., Scheuchl, B., and Rignot, E.: MEaSUREs Antarctic Boundaries for IPY 2007-2009 from Satellite Radar, Version 2. [Coastline, grounding line data]. Boulder, Colorado USA. NASA National Snow and Ice Data Center Distributed
1030   Active Archive Center. doi: https://doi.org/10.5067/AXE4121732AD, last accessed: 27 May 2021, 2017.

Moussavi, M., Pope, A., Halberstadt, A. R. W., Trusel, L. D., Cioffi, L., and Abdalati, W.: Antarctic Supraglacial Lake Detection Using Landsat 8 and Sentinel-2 Imagery: Towards Continental Generation of Lake Volumes, Remote Sens., 12, 134, https://doi.org/10.3390/rs12010134, 2020.

Müller, C. and Guido, S.: Introduction to Machine Learning with Python: A Guide for Data Scientists, O'Reilly Media, Inc.,
1035   Sebastopol, USA, 2016.

Munoz Sabater, J.: ERA5-Land hourly data from 1981 to present. Copernicus Climate Change Service (C3S) Climate Data Store (CDS): 10.24381/cds.e2161bac, last accessed: 14 March 2021, 2019.

NSIDC: The Antarctic 2020 to 2021 melt season in review: http://nsidc.org/greenland-today/2021/04/the-antarctic-2020-to-2021-melt-season-in-review/, last accessed: 23 June 2021, 2021.

1040   Padman, L., Costa, D. P., Dinniman, M. S., Fricker, H. A., Goebel, M. E., Huckstadt, L. A., Humbert, A., Joughin, I., Lenaerts, J. T. M., Ligtenberg, S. R. M., Scambos, T., and Broeke, M. R. van den: Oceanic controls on the mass balance of Wilkins Ice Shelf, Antarctica, J. Geophys. Res.-Oceans, 117, https://doi.org/10.1029/2011JC007301, 2012.

Reynolds, J. M.: Lakes on George VI Ice Shelf, Antarctica, Polar Rec., 20, 425–432, https://doi.org/10.1017/S0032247400003636, 1981.

1045   Reynolds, J. M. and Hambrey, M. J.: The structural glaciology of George VI Ice Shelf, Antarctic Peninsula, Brit. Antarct. Surv. B., 79, 79–95, 1988.

Rignot, E., Casassa, G., Gogineni, P., Krabill, W., Rivera, A., and Thomas, R.: Accelerated ice discharge from the Antarctic Peninsula following the collapse of Larsen B ice shelf, Geophys. Res. Lett., 31, https://doi.org/10.1029/2004GL020697, 2004.

1050   Rignot, E., Jacobs, S., Mouginot, J., and Scheuchl, B.: Ice-Shelf Melting Around Antarctica, Science, 341, 266–270, https://doi.org/10.1126/science.1235798, 2013.

Rignot, E., Mouginot, J., Scheuchl, B., Van den Broeke, M., Van Wessem, M., and Morlighem, M.: Four decades of Antarctic Ice Sheet mass balance from 1979–2017, PNAS, 116, 1095–1103, https://doi.org/10.1073/pnas.1812883116, 2019.

Rott, H., Abdel Jaber, W., Wuite, J., Scheiblauer, S., Floricioiu, D., Van Wessem, J. M., Nagler, T., Miranda, N., and Van den Broeke, M. R.: Changing pattern of ice flow and mass balance for glaciers discharging into the Larsen A and B embayments, Antarctic Peninsula, 2011 to 2016, The Cryosphere, 12, 1273–1291, https://doi.org/10.5194/tc-12-1273-2018, 2018.

Scambos, T. A., Bohlander, J. A., Shuman, C. A., and Skvarca, P.: Glacier acceleration and thinning after ice shelf collapse in the Larsen B embayment, Antarctica, Geophys. Res. Lett., 31, https://doi.org/10.1029/2004GL020670, 2004.

Shen, Q., Wang, H., Shum, C. K., Jiang, L., Hsu, H. T., and Dong, J.: Recent high-resolution Antarctic ice velocity maps reveal increased mass loss in Wilkes Land, East Antarctica, Sci. Rep, 8, https://doi.org/10.1038/s41598-018-22765-0, 2018.

Spergel, J. J., Kingslake, J., Creyts, T., Wessem, M. van, and Fricker, H. A.: Surface meltwater drainage and ponding on Amery Ice Shelf, East Antarctica, 1973–2019, J. Glaciol., 1–14, https://doi.org/10.1017/jog.2021.46, 2021.

Stokes, C. R., Sanderson, J. E., Miles, B. W. J., Jamieson, S. S. R., and Leeson, A. A.: Widespread distribution of supraglacial lakes around the margin of the East Antarctic Ice Sheet, Sci. Rep, 9, 1–14, https://doi.org/10.1038/s41598-019-50343-5, 2019.

Tetzner, D., Thomas, E., and Allen, C.: A Validation of ERA5 Reanalysis Data in the Southern Antarctic Peninsula—Ellsworth Land Region, and Its Implications for Ice Core Studies, Geosciences, 9, 289, https://doi.org/10.3390/geosciences9070289, 2019.

The IMBIE Team: Mass balance of the Antarctic Ice Sheet from 1992 to 2017, Nature, 558, 219–222, https://doi.org/10.1038/s41586-018-0179-y, 2018.

Tong, X., Liu, S., Li, R., Xie, H., Liu, S., Qiao, G., Feng, T., Tian, Y., and Ye, Z.: Multi-track extraction of two-dimensional surface velocity by the combined use of differential and multiple-aperture InSAR in the Amery Ice Shelf, East Antarctica, Remote Sens. Environ., 204, 122–137, https://doi.org/10.1016/j.rse.2017.10.036, 2018.

Trusel, L. D., Frey, K. E., Das, S. B., Karnauskas, K. B., Kuipers Munneke, P., van Meijgaard, E., and van den Broeke, M. R.: Divergent trajectories of Antarctic surface melt under two twenty-first-century climate scenarios, Nat. Geosci., 8, 927–932, https://doi.org/10.1038/ngeo2563, 2015.

Tuckett, P. A., Ely, J. C., Sole, A. J., Livingstone, S. J., Davison, B. J., Wessem, J. M. van, and Howard, J.: Rapid accelerations of Antarctic Peninsula outlet glaciers driven by surface melt, Nat. Commun., 10, 1–8, https://doi.org/10.1038/s41467-019-12039-2, 2019.

Turton, J. V., Kirchgaessner, A., Ross, A. N., King, J. C., and Kuipers Munneke, P.: The influence of föhn winds on annual and seasonal surface melt on the Larsen C Ice Shelf, Antarctica, The Cryosphere, 14, 4165–4180, https://doi.org/10.5194/tc-14-4165-2020, 2020.

Urraca, R., Huld, T., Gracia-Amillo, A., Martinez-de-Pison, F. J., Kaspar, F., and Sanz-Garcia, A.: Evaluation of global horizontal irradiance estimates from ERA5 and COSMO-REA6 reanalyses using ground and satellite-based data, Solar Energy, 164, 339–354, https://doi.org/10.1016/j.solener.2018.02.059, 2018.

Wachter, P., Beck, C., Philipp, A., Höppner, K., and Jacobeit, J.: Spatiotemporal Variability of the Southern Annular Mode and its Influence on Antarctic Surface Temperatures, J. Geophys. Res., 125, e2020JD033818, https://doi.org/10.1029/2020JD033818, 2020.

Wagner, A. C.: Flooding of the ice shelf in George VI Sound, Brit. Antarct. Surv. B., 28, 71–74, 1972.

Wessel, B., Huber, M., Wohlfart, C., Bertram, A., Osterkamp, N., Marschalk, U., Gruber, A., Reuß, F., Abdullahi, S., Georg, I., and Roth, A.: TanDEM-X PolarDEM 90 of Antarctica: Generation and error characterization, The Cryosphere Discussions, 1–30, https://doi.org/10.5194/tc-2021-19, 2021.

van Wessem, J. M., van de Berg, W. J., Noël, B. P. Y., van Meijgaard, E., Amory, C., Birnbaum, G., Jakobs, C. L., Krüger, K., Lenaerts, J. T. M., Lhermitte, S., Ligtenberg, S. R. M., Medley, B., Reijmer, C. H., van Tricht, K., Trusel, L. D., van Ulft, L. H., Wouters, B., Wuite, J., and van den Broeke, M. R.: Modelling the climate and surface mass balance of polar ice sheets using RACMO2 – Part 2: Antarctica (1979–2016), The Cryosphere, 12, 1479–1498, https://doi.org/10.5194/tc-12-1479-2018, 2018.